The Astrophysical Journal, 719:1503–1525, 2010 August 20 doi:10.1088/0004-637X/719/2/1503

THE PERSISTENCE OF COOL GALACTIC WINDS IN HIGH STELLAR MASS GALAXIES BETWEEN $z \sim 1.4$ AND $\sim$1*

Kate H. R. Rubin[1], Benjamin J. Weiner[2], David C. Koo[1], Crystal L. Martin[3,6], J. Xavier Prochaska[1], Alison L. Coil[4], and Jeffrey A. Newman[5]

[1] University of California Observatories, University of California, Santa Cruz, CA 95064, USA; rubin@ucolick.org
[2] Steward Observatory, 933 North Cherry Street, University of Arizona, Tucson, AZ 85721, USA
[3] Department of Physics, University of California, Santa Barbara, CA 93106, USA
[4] Department of Physics, University of California, San Diego, CA 92093, USA
[5] Department of Physics and Astronomy, University of Pittsburgh, Pittsburgh, PA 15260, USA
Received 2009 October 26; accepted 2010 June 23; published 2010 July 30

ABSTRACT

We present an analysis of the Mg II $\lambda\lambda$2796, 2803 and Fe II $\lambda\lambda$2586, 2600 absorption line profiles in co-added spectra of 468 galaxies at $0.7 < z < 1.5$. The galaxy sample, drawn from the Team Keck Treasury Redshift Survey of the GOODS-N field, has a range in stellar mass (M_*) comparable to that of the sample at $z \sim 1.4$ analyzed in a similar manner by Weiner et al. (W09), but extends to lower redshifts and has specific star formation rates which are lower by $\sim$0.6 dex. We identify outflows of cool gas from the Doppler shift of the Mg II absorption lines and find that the equivalent width (EW) of absorption due to outflowing gas increases on average with M_* and star formation rate (SFR). We attribute the large EWs measured in spectra of the more massive, higher-SFR galaxies to optically thick absorbing clouds having large velocity widths. The outflows have hydrogen column densities $N(\mathrm{H}) \gtrsim 10^{19.4}$ cm^{-2} and extend to velocities of $\sim$500 km s^{-1}. While galaxies with SFR $> 10\ M_\odot$ yr^{-1} host strong outflows in both this and the W09 sample, we do not detect outflows in lower-SFR (i.e., $\log M_*/M_\odot \lesssim 10.5$) galaxies at lower redshifts. Using a simple galaxy evolution model that assumes exponentially declining SFRs, we infer that strong outflows persist in galaxies with $\log M_*/M_\odot > 10.5$ as they age between $z = 1.4$ and $z \sim 1$, presumably because of their high absolute SFRs. Finally, our spectral analysis, combined with high-resolution *Hubble Space Telescope*/Advanced Camera for Surveys imaging, weakly suggests that outflow absorption strength increases with galaxy SFR surface density.

Key words: galaxies: evolution – galaxies: ISM – ultraviolet: ISM

Online-only material: color figures

1. INTRODUCTION

Galactic-scale gaseous outflows are a basic element of the process of galaxy evolution, and are observed in galaxies in the local universe and out to $z \sim 6$ (e.g., Heckman et al. 2000; Frye et al. 2002; Ajiki et al. 2002; Shapley et al. 2003; Martin 2005; Rupke et al. 2005b; Veilleux et al. 2005; Weiner et al. 2009). They are invoked to explain a wide variety of observational and theoretical results concerning the evolving stellar and gaseous content of dark matter halos. Outflows are a key component of the theory of merger-driven galaxy evolution, in which the primary mechanism driving the observed increase in the number density of "red and dead" galaxies from $z \sim 1$ to today is the merging of gas-rich blue galaxies (e.g., Faber et al. 2007; Tremonti et al. 2007; Hopkins et al. 2008; Sato et al. 2009). The removal (i.e., outflow) of gas is an expected consequence of merging and is a favored means by which star formation is subsequently quenched in the remnant. Outflows must be incorporated into models of disk galaxy formation which reproduce the observed scaling relations between disk rotation velocity, stellar mass (M_*), and radius (e.g., Dutton & van den Bosch 2009). Finally, galactic winds may give rise to the Mg II-absorbing gas in the extended gaseous halos around galaxies observed along quasi-stellar object (QSO) sightlines. Several lines of evidence support this idea (e.g., Bond et al. 2001; Bouché et al. 2006, 2007; Ménard & Chelouche 2009); however, alternative origins for this gas have also been suggested, i.e., multiphase cooling of hot halo gas, accretion of cold gas from the intergalactic medium, or tidal stripping (Maller & Bullock 2004; Tinker & Chen 2008; Wang 1993).

Detailed theoretical models for the physical mechanisms driving galactic outflows have been developed in the literature over the last several decades. In the "energy-driven" wind paradigm, supernova explosions or active galactic nucleus (AGN) feedback heat the surrounding gas and may displace both hot and cool gas originating in the interstellar medium (ISM), possibly removing it to the galactic halo or beyond. Momentum deposition from radiation or cosmic-ray pressure may also contribute to the acceleration of cool ISM gas; however, the relative importance of these two processes remains controversial (Dekel & Silk 1986; Strickland & Stevens 2000; Murray et al. 2005; Socrates et al. 2008; Strickland & Heckman 2009). In galaxies that are known to host outflows in the local universe, the hot phase is observed in X-ray emission, while the cooler phase is detected via optical emission lines (e.g., Hα, [N II] $\lambda\lambda$6548, 6583) and in absorption against the stellar continuum. In spite of this theoretical and observational work, it remains difficult to predict whether galactic winds will form and whether they will affect the kinematics of the ISM in a given galaxy. Theoretical studies propose that there is a "threshold" star formation rate (SFR) surface density (Σ_{SFR}) below which supernova-driven superbubbles cannot break out of a galactic disk and form a wind (e.g., McKee & Ostriker 1977).

* Some of the data presented herein were obtained at the W. M. Keck Observatory, which is operated as a scientific partnership among the California Institute of Technology, the University of California, and the National Aeronautics and Space Administration. The Observatory was made possible by the generous financial support of the W. M. Keck Foundation.
[6] Packard Fellow.

Observational constraints on the value of a universal threshold Σ_{SFR} remain merely suggestive (e.g., Lehnert & Heckman 1996; Martin 1999; Heckman 2002; Dahlem et al. 2006).

For instance, several studies have identified outflows in galaxies in which absorption line transitions tracing cool gas are blueshifted with respect to the systemic velocity. The Na I D λλ5890, 5896 doublet traces the kinematics and column of gas at $T \sim$ 100–1000 K, revealing outflows in local dwarf starbursts (Schwartz & Martin 2004) and luminous infrared galaxies (LIRGs) out to $z \sim 0.5$ (Heckman et al. 2000; Martin 2005; Rupke et al. 2005b). UV spectroscopy of both low- and high-ionization transitions such as Si II λ1260 and C IV λλ1548, 1550 in Lyman Break Galaxies (LBGs) at $z \sim 3$ has uncovered outflows of hundreds of km s^{-1} (e.g., Shapley et al. 2003) in these objects. All of these galaxies have high spatial concentrations of star formation, with $\Sigma_{SFR} > 0.1\,M_\odot$ yr^{-1} kpc^{-2} (Heckman 2002); the nearby galaxies have Σ_{SFR} values among the largest in the local universe. If there is a "threshold" Σ_{SFR} required to drive outflows, this suggests that it is likely equal to or below $0.1\,M_\odot$ yr^{-1} kpc^{-2} for local galaxies. The value of a threshold Σ_{SFR} for galaxies in the distant universe remains poorly constrained, although the high Σ_{SFR} ($>1\,M_\odot$ yr^{-1} kpc^{-2}) values in LBGs (Steidel et al. 1996; Meurer et al. 1997) suggest a similarly low threshold at $z \sim 3$.

Not only are outflows expected to contribute to increased numbers of post-merger, "quenched" red galaxies, but they may also influence the gradual decline of star formation since $z \sim 1$ among blue galaxies (Noeske et al. 2007b; Sato et al. 2009), as this decline is likely driven by gas exhaustion. The presence of winds in both distant star-forming and red sequence galaxies has been established (e.g., Sato et al. 2009; Weiner et al. 2009, hereafter W09), although the coevolution of outflows with the buildup of M_* and the decreasing cosmic SFR density (e.g., Hopkins 2004) remains unexplored at $z \gtrsim 0.5$.

We use a sample of 468 galaxies at $0.7 < z < 1.5$ drawn from the Team Keck Treasury Redshift Survey (TKRS; Wirth et al. 2004) of the GOODS-N field to examine the kinematics of cool ($T \lesssim 10^4$ K) gas traced by Mg II and Fe II absorption in co-added spectra. Because LIRG-like levels of star formation occur in most massive star-forming galaxies at $z \sim 1$ (Le Floc'h et al. 2005; Noeske et al. 2007b), and because cool outflows are common among LIRGs in the local universe, the galaxies in our sample are prime candidates for hosting outflows (Rupke et al. 2005b; Heckman et al. 2000). Indeed, W09 showed via analysis of co-added spectra of ∼1400 blue, star-forming galaxies at $z \sim 1.4$ that outflows traced by Mg II absorption are very common among the objects in their sample, and further demonstrated that outflow velocities and absorption strengths increase with both M_* and SFR over the ranges $9.5 < \log M_*/M_\odot < 10.8$ and $10\,M_\odot$ yr^{-1} < SFR < $50\,M_\odot$ yr^{-1}.

However, additional evidence indicates that the outflows observed in galaxies at $z \sim 1.4$ by W09 must cease at later epochs. W09 suggest that many of the galaxies in their sample will evolve into massive spirals (rather than ellipticals) at $z \sim 0$ (Blanton 2006; Noeske et al. 2007a). Sato et al. (2009), in a study of Na I kinematics in both star-forming and quiescent, red-sequence galaxies at $0.11 \leqslant z \leqslant 0.54$, *do not* detect outflows with velocities >50 km s^{-1} in a significant fraction (20%) of the blue cloud galaxies in their sample. Although the Sato et al. (2009) sample of blue cloud galaxies is incomplete, this suggests that at least some star-forming galaxies at $z \sim 1.4$ cease to drive winds in the redshift range $0.5 < z < 1.4$.

We use our sample to explore the dependence of the equivalent width (EW) of absorption due to outflowing gas on galaxy M_* and SFR and examine the relative importance of these two properties in determining outflow absorption strength among star-forming objects. We follow the coevolution of outflows, galaxy M_* and SFR in the range $0.7 \lesssim z \lesssim 1.4$ and search for the expected decline in outflow EW with increasing galaxy age. Finally, using co-added spectra in concert with the deep *Hubble Space Telescope*/Advanced Camera for Surveys (*HST*/ACS) imaging available in the GOODS-N field, we study the relationship between Σ_{SFR} and the EW of absorption due to cool outflows for the first time beyond the local universe.

We describe our sample, spectroscopy and imaging data in Section 2. We show evidence for outflow in a few individual galaxy spectra and in a co-added spectrum in Section 3, and describe the measurements we use to quantify outflow properties in Section 4. Section 5 describes our measurements of galaxy properties, and Section 6 examines trends in outflow properties with galaxy SFR, M_*, SFR surface density (Σ_{SFR}) and redshift. Section 7 discusses Fe II absorption properties. Sections 8 and 9 contain a discussion of these results and our conclusions. We adopt a ΛCDM cosmology with $H_0 = 70$ km s^{-1} Mpc^{-1}, $\Omega_M = 0.3$, and $\Omega_\Lambda = 0.7$. Magnitudes quoted are in the AB system unless otherwise specified, and stellar masses are reported in units of $M_\odot$.

2. DATA, SAMPLE, AND STACKING TECHNIQUE

2.1. Spectra

We use publicly available spectra from the TKRS (Wirth et al. 2004) for analysis of Mg II and Fe II kinematics. In brief, the TKRS is a magnitude-limited spectroscopic survey of galaxies selected to have $R_{AB} < 24.4$ in the GOODS-N field. Spectra were obtained using 1 hr exposures with DEIMOS (Faber et al. 2003) on the Keck 2 Telescope. The 600 l mm^{-1} grating blazed at 7500 Å was used with a 1″ wide slit. Spectra have a resolution of $\sigma_{inst} = 1.4$ Å (Weiner et al. 2006) and cover ∼4600–9800 Å with 0.648 Å pixel^{-1}. Approximately 1440 spectra of galaxies and AGNs were obtained in total.

The spectra were reduced using an early version of the pipeline developed by the DEEP2 Redshift Survey Team (Coil et al. 2004; J. A. Newman et al. 2010, in preparation). To determine first pass redshifts, the pipeline calculated the best-fitting source spectrum at each lag position, or redshift, from a linear combination of several template eigenspectra (Strauss et al. 2002; Glazebrook et al. 1998). The template spectra included stars, galaxy absorption and emission line spectra, and an AGN spectrum. The 10 best fits (i.e., those with the smallest χ^2 values) were saved, and members of the TKRS team then visually checked the best solution, replacing it in some cases, and assigned it a quality code. Wirth et al. (2004) performed a detailed comparison between TKRS redshift determinations and redshifts measured in other surveys, and estimated that the uncertainty in TKRS redshifts is ∼100 km s^{-1} or better.

We limit our sample to spectra with high redshift quality codes, i.e., with confidence level >90%, and with coverage of the Mg II λλ2796, 2803 doublet. We then visually inspect each of these spectra to check for broad Mg II emission lines; we exclude four objects with broad emission from our analysis (with object IDs 5609, 3660, 1488, and 9377). These cuts limit the sample size to 625 objects.

As noted in Cowie & Barger (2008), some of the TKRS spectra suffer from poor sky subtraction, and spectra of faint

objects can have negative continua. This implies that there are large systematic errors not accounted for in the one-dimensional error array for each spectrum. If the distribution of the errors in the estimates of the sky level were symmetric, the sky subtraction errors would not affect our results, as we work primarily with co-added spectra. However, while negative continua (i.e., oversubtractions) occur preferentially when there is excess scattered light in a given slit, undersubtraction does not likely result from a specific systematic issue. Thus, we expect that overestimation of the sky level is more likely to occur than underestimation in general. Including the objects with oversubtracted sky in co-added spectra will tend to reduce the continuum level of the co-add. We exclude the 96 spectra with a negative median continuum level measured between rest wavelengths 2790 Å and 2810 Å (i.e., 15% of the sample). This method of tagging spectra with poor sky subtraction is almost certainly not comprehensive; however, it likely removes the worst cases from the sample.

Among the remaining 529 spectra, a few have very poor wavelength solutions in the blue due to the paucity of arc lamp lines at $\lambda < 5000$ Å. This may affect the accuracy of the redshift determination as well as the offset of UV absorption lines from systemic velocity. In order to assess the quality of the wavelength solutions, we fit a single Gaussian to the [N I] sky lines at 5197 Å and 5200 Å, which are not resolved in the TKRS spectra. We define $v = 0$ km s^{-1} to be at the average of the true wavelengths of the two lines ($\langle\lambda_{5197,5200}\rangle$) and measure the velocity offset of the sky line complex in each spectrum. Our assumption that the wavelength centroid of a single Gaussian fit to the blended lines is equal to the average of their central wavelengths holds if the lines have equal strengths. However, the ratio of the statistical weights of the upper energy levels and the Einstein coefficients for the two transitions indicate that their amplitude ratio ($A(5200)/A(5197)$) must vary between 1.5 (at low density) and 0.65 (at high density). Given the velocity resolution of the spectra, $\sigma_{\rm inst} = 1.4$ Å, the fit of a single Gaussian model to the sum of two Gaussians with this range in amplitude ratios yields a range in centroid velocities between -19 km s^{-1} and 18 km s^{-1} measured with respect to $\langle\lambda_{5197,5200}\rangle$. To find the mean velocity offset of the sky line complex for the sample ($\langle v_{\rm obs,5197+5200}\rangle$), we first exclude spectra with sky lines offset by more than 200 km s^{-1} from $\langle\lambda_{5197,5200}\rangle$, and then calculate the mean of the velocity offset in the remaining spectra. The resulting $\langle v_{\rm obs,5197+5200}\rangle$ is 13 km s^{-1}. We then exclude all spectra from the sample (57 objects) with sky lines offset by more than 130 km s^{-1} from $\langle v_{\rm obs,5197+5200}\rangle$. Accounting for variations in the relative strengths of the sky lines, this means that all remaining 472 spectra have sky lines offset by no more than 162 km s^{-1} from their true central wavelengths. After eliminating four additional objects, which lack the supplementary measurements discussed in Section 5, we have a final sample size of 468. Figure 1 shows the redshift distribution of the objects in the sample, which has a median redshift $z = 0.94$.

The standard deviation of the distribution in sky line velocity offsets for spectra remaining in the sample is 40 km s^{-1} (not accounting for variations in the strengths of the sky lines). This dispersion measures the typical wavelength uncertainty in the TKRS spectra at $\lambda_{\rm obs} \sim 5200$ Å. We estimate considerably smaller uncertainties at redder wavelengths, as arc lines are more abundant in this range. For instance, a Gaussian fit to the sky line at 5577 Å yields maximum velocity offsets <30 km s^{-1} and a dispersion of 10 km s^{-1} for the spectra in the sample.

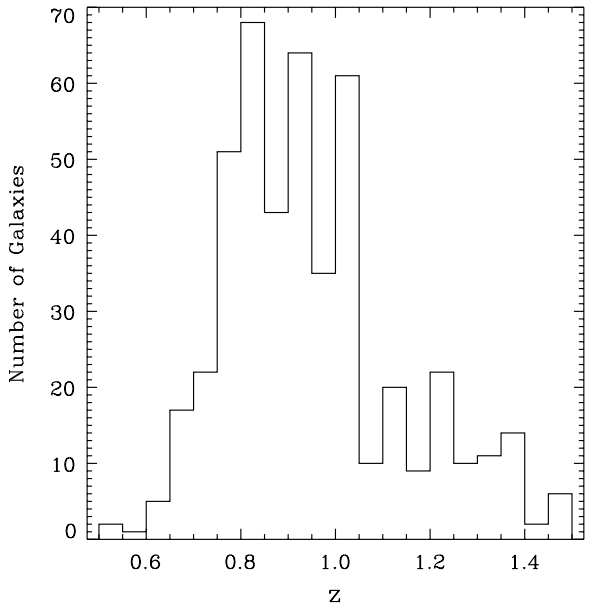

Figure 1. Histogram showing redshift distribution of all 468 galaxies included in our analysis in bins of $\Delta z = 0.05$. Only spectra with coverage of Mg II λλ2796, 2803 are included, which places a lower bound on the redshift distribution at $z \approx 0.7$.

The errors in the wavelength solution introduce uncertainties in the systemic velocities of the UV absorption lines in each spectrum. Throughout the paper, we assume that the systemic velocity of each galaxy is given by the TKRS redshift. As redshift determinations are most strongly dependent on sections of the spectra redward of observed wavelength $\lambda_{\rm obs} \sim 5577$ Å in the redshift range of our sample, they should not be affected by poor blue wavelength solutions. However, the UV absorption lines of interest are blueward of $\lambda_{\rm obs} \sim 5577$ Å in the redshift range $z < 1$ in the case of Mg II and in the range $z < 1.15$ in the case of Fe II. We estimate the error in the systemic velocity for these transitions by assuming the wavelength solution is perfect at $\lambda_{\rm obs} \sim 5577$ Å and that it varies linearly to the blue, with absolute velocity offsets at $\lambda_{\rm obs} \sim 5200$ Å between 20 km s^{-1} and 162 km s^{-1}. At the very bluest wavelengths, the velocity offset is <135 km s^{-1} for sky line velocity offsets <40 km s^{-1} and has a maximum of 546 km s^{-1} for sky line velocity offsets of 162 km s^{-1}. Near the median redshift of the sample ($z = 0.94$), the velocity offset at Mg II is ∼27 km s^{-1} for sky line velocity offsets of 40 km s^{-1}. These errors in the systemic velocities of UV absorption lines must be considered when interpreting results from co-added spectra, as discussed in Section 2.3.

2.2. Imaging

We use the high-quality *HST*/ACS imaging available in the GOODS-N field (Giavalisco et al. 2004). The imaging covers a $10' \times 16'$ area with the ACS *F435W*, *F606W*, *F775W*, and *F850LP* bands (B_{435}, V_{606}, i_{775}, and z_{850}). The limiting surface brightness at 1σ in a 1 arcsec^2 aperture in the *F850LP* band is $\mu_{AB} = 27.3$ mag arcsec^{-2} (Giavalisco et al. 2004, ver. 1 release). We use the mosaic data in each band with a pixel scale $0\farcs03$ pixel^{-1}.

2.3. Stacking Technique

We use the code written by J.A.N. to co-add TKRS spectra. The code first masks out bad pixels in each object spectrum. It then renormalizes each inverse variance array so that it has

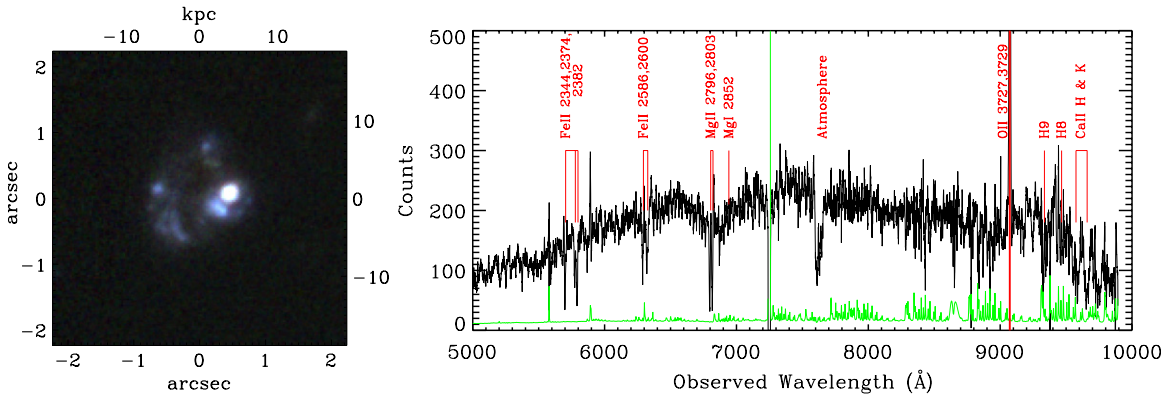

Figure 2. *HST*/ACS color image of TKRS2158 in the V_{606}, i_{775} and z_{850} bands (left) and the TKRS spectrum inverse-variance smoothed using a window of 9 pixels (right). The error in the smoothed spectrum is shown in green. The absorption feature at ∼7650 Å is due to the atmosphere. Absorption due to Mg II and Fe II is evident at observed wavelengths ∼5700–6900 Å. The mean S/N near the Mg II transition is 3.4 pixel^{-1}. The object has an irregular morphology with several bright blue knots, suggestive of a recent or ongoing merger.

(A color version of this figure is available in the online journal.)

a median equal to 1 and varies only due to sky features or bad pixels, and not due to variations in object flux. This is achieved by fitting a model for the variation of the inverse variance as a function of the night sky flux, which is stored with the extracted object spectrum. Each spectrum and its associated inverse variance array are linearly interpolated onto a grid of rest-frame wavelength and the spectra are co-added. The flux in each pixel is weighted by the renormalized inverse variance, so that pixels with more noise from sky emission are given less weight, while each spectrum overall contributes to the stack in proportion to its flux and is not given an extra weighting corresponding to its signal-to-noise ratio (S/N). This results in a co-add which is "light-weighted." This method of co-addition is the same as that used in W09.

Errors in TKRS redshifts as well as errors in the wavelength solutions will have the effect of broadening the absorption and emission features located at the true systemic velocity in the co-added spectra. The redshift uncertainties discussed above are <100 km s^{-1}, while velocity offsets due to poor wavelength solutions are estimated to be <135 km s^{-1} for the 68% of the spectra with the smallest sky line velocity offsets, making the extreme assumption that the UV absorption lines of interest are always at the bluest end of the wavelength coverage. We therefore expect that absorption observed at velocities offset from systemic by $\gtrsim$200 km s^{-1} in both the Mg II and Fe II transitions in a given co-add is most likely due to absorption at velocities offset from the true systemic velocities of the galaxies in the sample.

3. REST-FRAME UV METAL-LINE ABSORPTION IN TKRS GALAXIES

3.1. Detection of Outflowing Gas in TKRS2158

The continuum S/N of a typical TKRS spectrum near Mg II is ∼1 pixel^{-1}. We are therefore not able to visually identify Mg II absorption in the vast majority of the individual spectra. There are a few brighter galaxies, however, for which rest-frame UV absorption lines are evident.

One example is shown in Figure 2, which includes a color *HST*/ACS image and the full spectrum of the object TKRS2158. This object has a redshift $z = 1.43339$, has absolute B-band magnitude $M_B = -22.99$ (Section 5.1), and has an infrared luminosity $\log L_{IR}/L_{\odot} = 11.9$ (Melbourne et al. 2005).

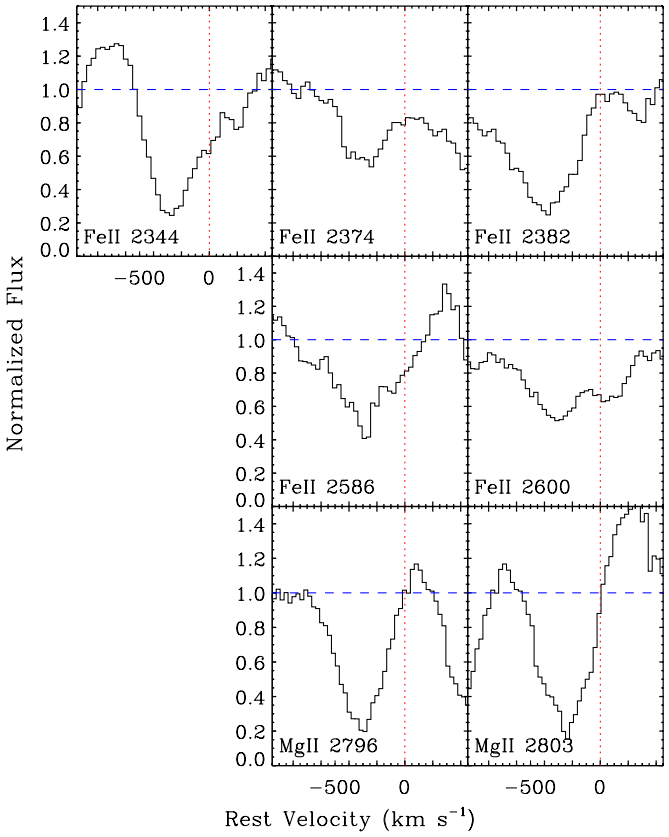

Figure 3. UV absorption lines in the spectrum of TKRS2158. The spectrum has been inverse-variance smoothed using a window of 9 pixels. The systemic velocity is marked with vertical dotted lines and the dashed lines mark the continuum level. All absorption lines shown are blueshifted by at least ~ -230 km s^{-1}. Narrow redshifted emission is evident in the Mg II transition, resulting in a P Cygni-like line profile.

(A color version of this figure is available in the online journal.)

Figure 3 includes sections of the same spectrum showing UV absorption line profiles. The systemic velocity is given by the redshift of the galaxy reported in the TKRS, which was calculated as described in Section 2.1. The fit of the template spectra used in the redshift determination was likely dominated by the velocity of the [O II] doublet. Not only are Mg II λλ2796, 2803 and Fe II λλ2586, 2600 absorption lines detected,

Table 1
Measurements of UV Absorption Line EWs and Velocity Offsets in TKRS2158

Transition	EW (Å)	Δv (km s^{-1})
Fe II 2344	2.38 ± 0.37	−262 ± 29
Fe II 2374	1.76 ± 0.31	−281 ± 42
Fe II 2382	3.32 ± 0.38	−415 ± 36
Fe II 2586	1.99 ± 0.35	−287 ± 40
Fe II 2600	2.63 ± 0.39	−229 ± 62
Mg II 2796	2.92 ± 0.32	−314 ± 19
Mg II 2803	2.72 ± 0.32	−257 ± 30

Notes. Systemic velocities are determined using the template fitting procedure described in Section 2.1 and leverage the velocity of the [O II] emission line doublet. EWs have been measured using a feature-finding code discussed in Cooksey et al. (2008).

but Fe II λλ2344, 2374, 2382 absorption is evident further to the blue. We calculate boxcar EWs of these lines using a feature-finding code described in Cooksey et al. (2008).[7] We also measure velocity offsets of each line with respect to systemic by fitting a Gaussian to each and finding the offset of its centroid. These measurements are reported in Table 1. All lines are offset from the systemic velocity by ~ -250 km s^{-1}, with the exception of the Mg II 2796 line and the Fe II 2382 line, which are offset -314 ± 19 km s^{-1} and -415 ± 36 km s^{-1}, respectively. These kinematics clearly indicate an outflow of cool gas from this galaxy. Discrepancies in the measurements of the velocity offsets could be due to noise in the spectrum, such as poorly subtracted sky emission at the locations of certain absorption lines. Additionally, narrow emission in the Mg II 2796 transition or in Fe II* fine-structure transitions may be filling in some of the absorption profiles and shifting their centers to the blue (e.g., Rubin et al. 2010).

Figure 4 shows the spectral regions around the UV absorption lines for several more individual TKRS objects. Blueshifted absorption lines are evident in a few of these spectra, hinting at the presence of outflows. However, most of the spectra are not of sufficiently high quality to reliably measure velocity offsets or line strengths for individual galaxies.

3.2. Outflow Signature in Co-added Spectra

Figure 5 shows sections of the co-add of the full galaxy sample (468 objects) surrounding the Mg II and Mg I λ2852 absorption lines in black. The spectrum has been normalized by a linear fit to the continuum flux in the continua regions -2400 km s^{-1} $< v < -1600$ km s^{-1} and 800 km s^{-1} $< v <$ 1600 km s^{-1}, where $v = 0$ km s^{-1} at 2803.531 Å and 2852.964 Å for Mg II and Mg I, respectively. This continuum normalization is applied to all co-adds presented. The Mg II line profiles in this figure are asymmetric, with more absorption on the blue side of $v = 0$ km s^{-1}. The Mg I absorption line is asymmetric in the same sense. Quantitative analysis of these lines will be performed in later sections.

To test whether the properties of the co-add reflect the properties of most of the individual galaxies in the sample, rather than a few of the brightest galaxies, we measure the flux in various velocity ranges with respect to Mg II λ2803 in individual spectra. This was done in W09 and our velocity windows match those used in that work: 400 km s^{-1} $< v <$ 800 km s^{-1} (window 1), and -150 km s^{-1} $< v < -50$ km s^{-1} (window 2). Window 1 provides a measurement of the continuum, and window 2 probes the flux in the deepest part of the blueshifted 2803 Å line (although this velocity range may not probe blueshifted absorption in all spectra, due to errors in systemic velocity determinations as discussed in Section 2.3). We plot the average number of counts per pixel weighted by the inverse variance in window 2 versus window 1 in the top panel of Figure 6. This shows that many of the spectra have a count decrement in window 2 (where blueshifted absorption is expected) relative to window 1 (where we are making a measurement of the counts in the continuum). Sixty-seven percent of the spectra have average counts lower in window 2 than in window 1, indicating that a majority of the spectra contribute to the co-added flux decrement blueward of systemic velocity.

We also wish to test for the presence of emission in the Mg II transition in individual galaxy spectra. This is motivated by the work of W09, who identify Mg II emission in co-added spectra as well as in ∼4% of the individual galaxy spectra in their

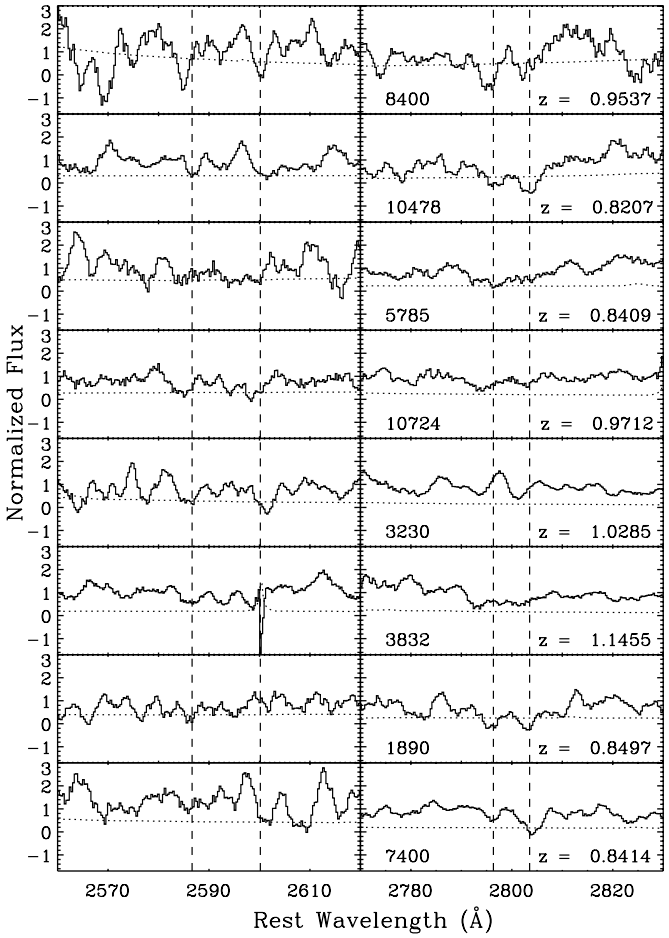

Figure 4. Portions of TKRS spectra covering the Fe II λλ2586, 2600 and Mg II λλ2796, 2803 transitions, inverse-variance smoothed using a 9 pixel window and normalized to the continuum level. The systemic velocity of each transition is marked with dashed lines. Objects are arranged from top to bottom in order of increasing apparent R magnitude (Wirth et al. 2004), and the TKRS ID numbers are given in the right-hand panel. The Mg II line profiles in the spectra of objects 8400 and 1890 are blueshifted with respect to systemic velocity, suggesting the presence of outflows. Dotted lines show the error in each pixel.

[7] We use the "doublet ratio" method described in Section 8.1 to estimate the column density of the gas traced by Mg II absorption in this spectrum. The EWs listed in Table 1 yield a doublet ratio of 1.07 ± 0.17, corresponding to a lower limit on the optical depth in the 2803 Å line of 3.1. The resulting log N(Mg II) > 14.5, or log N(H) > 20.2, under the assumption of solar abundances, no ionization correction, and a factor −1.3 dex Mg dust depletion.

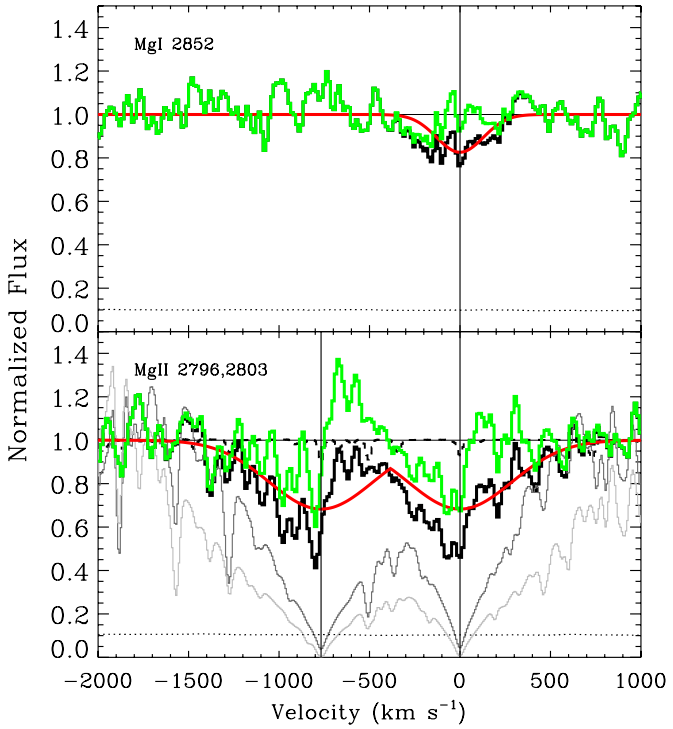

Figure 5. Sections of the co-add of the full sample around Mg II and Mg I. The co-add has been normalized to the level of the continuum surrounding the absorption lines as described in the text and is plotted in thick black. The dotted line is the error array for the co-add and the black vertical lines mark the systemic velocity for each transition. The red line overplotted on the co-add shows the Gaussian fits to the red sides of the 2803 Å and 2852 Å lines; the Gaussian model profile for the systemic absorption in the 2803 Å transition is assumed to describe the systemic absorption in the 2796 Å transition as well. The green spectrum shows the absorption remaining after the models have been divided out of the co-add. The black horizontal line marks the continuum level. The spectra shown with thin lines are UVBLUE theoretical spectra of an O star (dashed black; exhibits weak absorption features just below the horizontal line marking the continuum), an A star (solid gray), and a solar-type star (solid light gray) with $\log g = 4$–5.

(A color version of this figure is available in the online journal.)

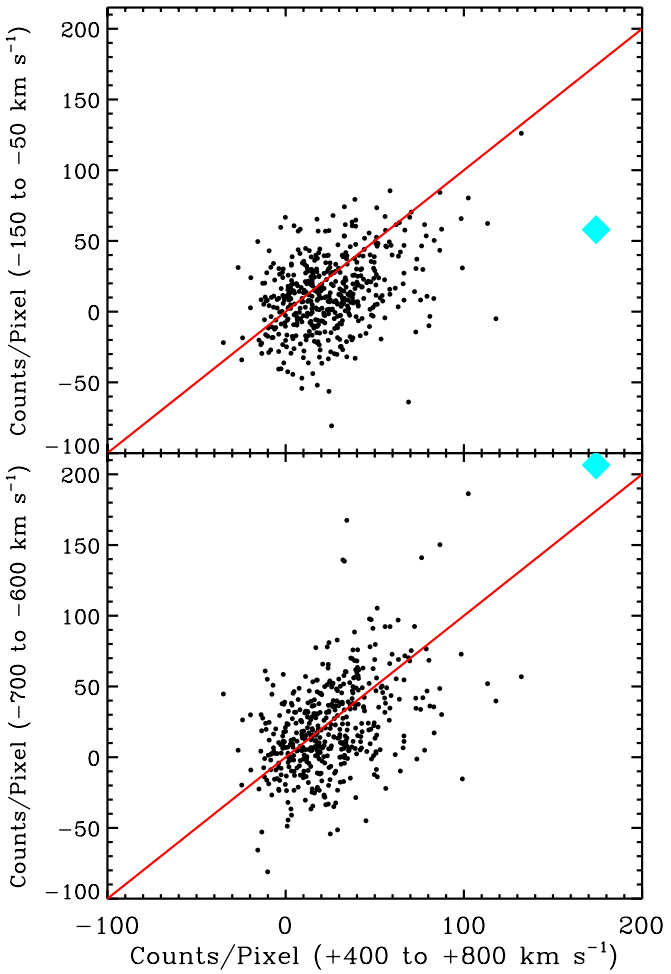

Figure 6. Top: average counts pixel^{-1} in window 2 vs. window 1. A one-to-one relation is shown in red. Sixty-seven percent of the spectra have lower average counts in window 2 vs. window 1; thus, a flux decrement to the blue of the 2803 Å line is a property of many of the galaxy spectra in the sample. Bottom: average counts pixel^{-1} in window 3 vs. window 1. The points are distributed approximately evenly across the line marking a one-to-one relation (red), with 46% of spectra lying above the line, indicating that for most spectra, the two windows include continuum emission with similar counts per pixel. Only a few objects are separated from the main locus with high values in window 3, indicating there are only a few objects with "excess emission." The location of the spectrum of TKRS2158 is marked in cyan in both panels.

(A color version of this figure is available in the online journal.)

sample at $z \sim 1.4$. This emission may be due to AGN activity, but could also be related to some other physical process. W09 attempted to exclude galaxies which exhibit Mg II emission from their analysis of outflow properties in co-added spectra, as the complicated continuum shape in these individual spectra makes characterization of the Mg II absorption line profiles in the co-adds difficult. To identify individual spectra with Mg II emission in our sample, we measure the flux level in the velocity range -700 km s^{-1} $< v < -600$ km s^{-1} (window 3) and compare it to our measurements for window 1 in the bottom panel of Figure 6. The placement of window 3 is immediately to the red of the 2796 Å line and samples the region between the absorption lines where Mg II emission is likely strongest. Points toward the upper part of this plot have "excess emission" in window 3. Overall, the points are distributed evenly across the line marking a one-to-one relation (i.e., with 46% of spectra lying above the line) indicating that the two windows tend to include continuum emission with similar count levels. There are seven spectra in our sample with counts pixel^{-1} in window 3 greater than 120. Four of these spectra have P Cygni-like line profiles at Mg II; the three remaining spectra are pushed into the "excess emission" regime by noise in the window. Removal of these spectra from our sample does not significantly affect the Mg II line profiles in the co-added spectrum shown in Figure 5. Their inclusion will therefore not demand careful modeling of emission in the continuum and we retain them in the following analysis.

4. ANALYSIS OF AVERAGE OUTFLOW PROPERTIES TRACED BY Mg II ABSORPTION

In this section, we introduce two measurements that will be used in the remainder of the paper to assess the strength of the absorption due to outflowing gas in co-added spectra. With both methods we attempt to estimate the strength of absorption at the systemic velocity through analysis of the red side of the Mg II 2803 line. We then "correct" the measurement of the absorption strength on the blue side of either the Mg II 2796 line or both Mg II lines accordingly. This corrected measurement should then depend only on the absorption strength of outflowing gas. The first method uses boxcar EWs for the measurements in each velocity range and is useful in the case of low S/N co-adds, while

the second includes more detailed fitting of the line profile. The latter method, however, requires that the red side of the Mg II 2803 line be well characterized by a Gaussian.

Analysis of the absorption strength of outflowing gas is complicated by absorption from stellar atmospheres and the ISM near the systemic velocity. Photospheric Mg II absorption at the systemic velocity is strongest in F8–G1 type stars (Kinney et al. 1993), in which the EW of the 2796 Å line can reach ∼7 Å (see Section 7). This is demonstrated in Figure 5, which shows theoretical stellar spectra of solar-metallicity dwarf O ($T_{\rm eff}$ = 42,500 K), A ($T_{\rm eff}$ = 8000 K), and G ($T_{\rm eff}$ = 6000 K) stars from the UVBLUE library with thin dashed black and solid gray lines (Rodríguez-Merino et al. 2005). These spectra have been continuum-normalized using the same method applied to the co-add. While the early-type stellar spectrum exhibits only weak absorption, the cooler stars produce strong, broad Mg II absorption lines. In addition, as discussed in W09, very bright late B, A, and F stars can exhibit asymmetric or shifted Mg II absorption due to stellar winds (Snow et al. 1994); these stellar absorption lines may be blueshifted by ~ -100 km s^{-1}, although this is not evident in the UVBLUE spectra, as the effects of winds are not included in these models. Additional absorption in the line profile may be due to the ISM of the galaxies. This gas is in the disks of the galaxies and will rarely be blueshifted by more than a few tens of km s^{-1} (i.e., in the case of a rotating disk). The situation for Mg I is simpler; stellar Mg I absorption is not blueshifted and is only found in the photosphere of F stars. It may be present in the ISM, however, and in outflowing gas.

4.1. Boxcar Method

In order to measure the amount of absorption due to outflowing gas in each co-add, we make the assumption that the Mg II doublet is saturated in our spectra near systemic velocity, such that the 2796 Å and 2803 Å lines have the same depths at v = 0 km s^{-1}. Mg II becomes saturated at column densities (N) $\approx 10^{14}$ cm^{-2}, which occur at relatively low hydrogen column densities $>10^{19}$ cm^{-2} at solar abundance. The ISM and stellar atmospheres, which likely dominate the absorption line profile near systemic velocity as discussed above, typically have columns exceeding this value. See Section 8.1 for further discussion of this issue. We measure $W_{\rm diff}$, where

$$W_{\rm diff} = W_{2796\ \text{Å, blue}} - W_{2803\ \text{Å, red}}, \quad (1)$$

and where

$$W_{2796\ \text{Å, blue}} = \sum_{v=-500\ \text{km s}^{-1}}^{0\ \text{km s}^{-1}} \left[1 - \frac{f(v)}{f_c(v)}\right] \Delta v, \quad (2)$$

$$W_{2803\ \text{Å,red}} = \sum_{v=0\ \text{km s}^{-1}}^{500\ \text{km s}^{-1}} \left[1 - \frac{f(v)}{f_c(v)}\right] \Delta v. \quad (3)$$

$W_{2803\ \text{Å,red}}$ quantifies the amount of absorption due to gas that is not outflowing, and we subtract it from $W_{2796\ \text{Å, blue}}$ to avoid overestimating the outflow absorption strength from the inclusion of absorption due to gas at $v \approx 0$ km s^{-1} associated with the ISM and/or stellar atmospheres.

4.2. Decomposition Method

In addition to the boxcar measurement discussed above, we also adopt the method of W09 to first remove the stellar and "stationary" ISM absorption from the line profile before making measurements of any outflow. We use the model presented in W09:

$$F_{\rm obs}(\lambda) = C(\lambda)(1 - A_{\rm sym}(\lambda))(1 - A_{\rm flow}(\lambda)), \quad (4)$$

$$A_{\rm sym}(\lambda) = A_{2796} G(v, \lambda_{2796}, \sigma) + A_{2803} G(v, \lambda_{2803}, \sigma), \quad (5)$$

where $F_{\rm obs}(\lambda)$ is the observed flux density, $C(\lambda)$ is the galaxy continuum emission, and $A_{\rm sym}(\lambda)$ and $A_{\rm flow}(\lambda)$ are the line profiles of the symmetric and blueshifted (outflowing) absorption. Here, we make no attempt to include emission in Mg II above the continuum in our model; this issue will be addressed in more detail in Section 4.4. $A_{\rm sym}(\lambda)$ is the sum of two Gaussians centered at the rest velocity of each line in the doublet. In order to calculate $A_{\rm sym}$, we fit a Gaussian profile to the red side (0 km s^{-1} $< v <$ 1600 km s^{-1}) of the 2803 Å and 2852 Å lines. See Figure 5 for a demonstration of this procedure. Because the Mg II doublet is blended in our spectra, we then simply impose the Gaussian fitted to the 2803 Å line onto the profile of the 2796 Å line. The depths of these two Gaussians are kept the same ($A_{2796} = A_{2803}$), since the Mg II lines are likely mostly saturated. It may be that the 2796 Å line is in fact slightly deeper than the 2803 Å line; in this case, we will underestimate the strength of the systemic absorption in this line. We divide the co-add by this model and show the resulting blueshifted (or outflowing) absorption line profile in Figure 5 in green.

We presume that this profile measures only absorption from gas that is outflowing. However, if the doublet ratio for the stationary absorption is larger than one, we will overestimate the absorption due to outflowing gas (and emission to the red of the 2796 Å line will be artificially weakened). Redshifted emission in the 2803 Å line also affects the amplitude and width of the Gaussian we fit to the absorption line profile, and can cause an overestimate of the EW of outflowing gas. Emission in the 2796 Å line (evident in Figure 5) may in turn cause us to underestimate the EW due to the outflow (see Section 4.4 for more discussion of these effects). Finally, we are assuming that little of the absorbing gas is flowing into the galaxies; if we were to detect a substantial inflow, we would overestimate the amount of absorption at the systemic velocity due to deeper profiles on the red sides of the lines and underestimate the EW of outflowing gas.

As can be seen in Figure 5, no absorption is evident at positive relative velocities in the line profile shown in green; i.e., the "outflow" profile. Some emission occurs on the red side of the 2796 Å line; this will be discussed in Section 4.4. The total EW, or "outflow EW," of the features measured between -1132 km s^{-1} $< v <$ 0 km s^{-1} with respect to the 2796 Å line and between -384 km s^{-1} $< v <$ 0 km s^{-1} with respect to the 2803 Å line using a boxcar sum is 1.13 ± 0.18 Å. Note that we include measurements for *both* of the lines in the doublet in the "outflow EW" and that W09 included a measurement for the 2796 Å line only. The velocity range over which we measure 2803 Å absorption is chosen to avoid including emission from the 2796 Å line in the outflow EW. Although the green profile for Mg I λ2852 is suggestive of an outflow, the outflow absorption is not formally detected and has a 3σ upper limit of ∼0.3 Å, possibly indicating that the outflow is dominated by gas densities lower than those which contain a significant column in Mg I (Murray et al. 2007).

To compute the error on the outflow EW, we first generate 1000 realizations of the symmetric absorption profile by adding noise to the best-fit symmetric model generated in the above

procedure. The level of the added noise is determined by the noise in the co-added spectrum. Each of these realizations is fit with a Gaussian and a double Gaussian profile ($A_{\rm sym}$) is created as above. We then calculate the standard deviation of the values of these 1000 different models at each pixel, which yields an estimate of the error introduced by the model fitting procedure as a function of velocity. This error is combined in quadrature with the error in the co-added spectrum itself, producing an error at each pixel in the outflow profile ($A_{\rm flow}$). It is then straightforward to use these errors to calculate the uncertainty in EW measurements of the outflow profile.

4.3. Sensitivity of $W_{\rm diff}$ and Outflow EW to Winds

We now explore the extent to which these two quantification methods are sensitive to outflows with a range of physical properties. To do this, we generate a series of model Mg II absorption line profiles, each with varying amounts of absorption at systemic velocity and offset to negative velocities. We model both the systemic absorption and the outflowing absorption as single velocity components with Gaussian optical depth (τ). While cool outflowing gas likely consists of multiple absorbing clouds at different velocities (e.g., Martin 2005), we are co-adding our data, and thus we expect that such features will be completely smoothed out. Components are parameterized following Rupke et al. (2005b), with variable Mg II column density (N(Mg II)), covering fraction (C_f), Doppler parameter (b_D), and central wavelength (λ_0). In all of our models, we choose N(Mg II)$= 10^{14.9}$ cm^{-2} for the systemic component, such that the profile is completely saturated, and N(Mg II) $= 10^{14}$ cm^{-2} for the outflowing component. All components (systemic and outflowing) have $C_f = 0.5$, close to the 55% absorption depth of the saturated Mg II profiles in W09 (which in co-added spectra corresponds to the detection frequency of outflows multiplied by the covering fraction of cool outflowing clouds). Outflowing components are given relative velocities of -100, -200, and -300 km s^{-1}; we also create models with no outflowing component. In each model, the systemic and outflowing components have the same b_D; however, we allow this parameter to have the values $b_D = 50$, 150, and 250 km s^{-1} in different models. We therefore have a grid of 3×4 models in b_D and outflow velocity space.

We smooth each of these models to the velocity resolution of the individual spectra, $\sigma_{\rm inst} = 1.4$ Å (Weiner et al. 2006), adjusted to the restframe at the median redshift of the sample ($z = 0.94$). A velocity resolution element in the co-added spectra is larger than this, due to uncertainties in the redshift determinations and wavelength solutions for the individual spectra (see Section 2.1); however, the results are similar if we repeat the analysis assuming a velocity resolution of $2\sigma_{\rm inst}$. After smoothing we add different levels of noise such that the resulting spectra have S/N = 3, 6, and 9 pixel^{-1}, consistent with the range in S/N levels of co-added spectra we create in Section 6 (see Table 2). We generate 1000 realizations of each model at each S/N level, and then measure $W_{\rm diff}$ and perform our decomposition analysis for each realization.

Figure 7 shows the distribution of the measured outflow EW and $W_{\rm diff}$ values for all models as a function of the model outflow velocity. The points have been offset by an arbitrary amount in velocity so that they do not overlap. The mean outflow EW and $W_{\rm diff}$ for models with S/N = 3 pixel^{-1}, 6 pixel^{-1}, and 9 pixel^{-1} are shown with cyan diamonds, blue circles, and black squares, respectively. The point size increases with b_D. The errorbars show the 90% confidence intervals in the measured quantities. The size of these intervals and the central values indicate the degree to which outflow EW and $W_{\rm diff}$ are successful in characterizing the underlying physical absorption profile. For instance, at S/N = 3 pixel^{-1}, $W_{\rm diff}$ and outflow EW have very broad distributions for all models. For models with no outflow, $W_{\rm diff}$ exceeds values of 0.5 Å in between 12% and 22% of realizations, and outflow EW exceeds values of 1.0 Å in 5%–27% of realizations. Likewise, models with outflows can have $W_{\rm diff}$ or outflow EW < 0.5 Å, although in general the distributions shift to higher values of these quantities as outflow velocities increase. We conclude, however, that when co-adds have S/N $\sim$ 3 pixel^{-1}, we are able to confirm the presence of outflows only if the measured values of outflow EW are $\gtrsim$1.8 Å and $W_{\rm diff}$ values are $\gtrsim$0.8 Å. These values are recovered for outflow velocities $\gtrsim$100 km s^{-1} and occur more frequently with higher b_D. If lower values are measured, the presence or lack of outflows remains ambiguous.

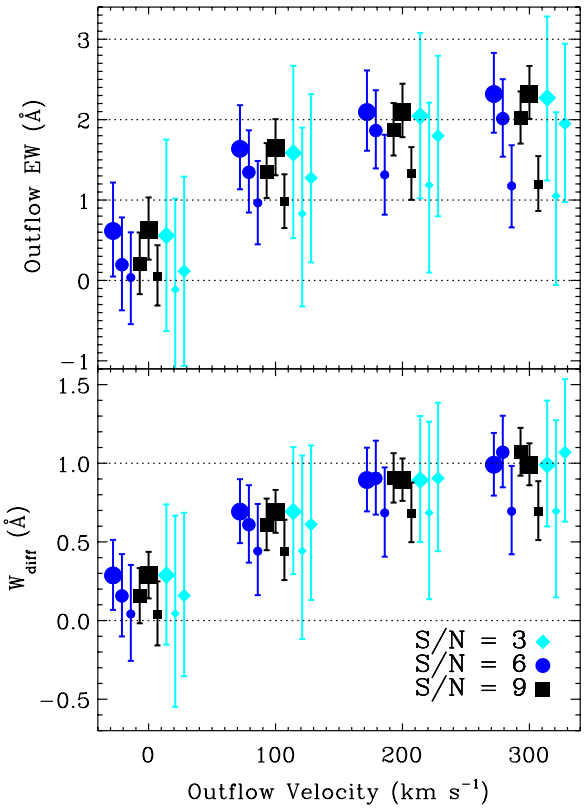

Figure 7. Top: distribution in measured outflow EW values for model spectra as a function of the input outflow velocity. The points are offset slightly in velocity to prevent overlap. The mean outflow EW for realizations with S/N = 3 pixel^{-1}, 6 pixel^{-1}, and 9 pixel^{-1} are shown with cyan diamonds, blue circles, and black squares, respectively. Small, medium, and large symbols show results for models with $b_D = 50$, 150, and 250 km s^{-1}. The errorbars indicate the 90% confidence intervals for each set of model realizations. Bottom: same as above, for $W_{\rm diff}$. (A color version of this figure is available in the online journal.)

These measurements become more sensitive with increasing S/N. At S/N = 6 pixel^{-1}, $W_{\rm diff}$ can be as high as 0.5 Å and outflow EW as high as 1.2 Å for models with no outflow. However, models with outflows yield mean values higher than these if $b_D = 150$ or 250 km s^{-1}. Values of outflow EW > 1.4 Å are measured for at least 95% of realizations of models with high values of b_D and outflow velocity. At S/N = 9 pixel^{-1}, models with no outflow have $W_{\rm diff}$ and outflow EW $\lesssim 0.4$ and 1.0 Å, respectively, while models with outflows and $b_D = 150$ or 250 km s^{-1} again yield higher values

in at least 96% of realizations. Models with $b_D = 50$ km s^{-1} have higher mean values if the outflow velocity $\gtrsim$200 km s^{-1}.

In the remaining text, we often refer to the "strength" of the outflows exhibited by a given subset of our spectral sample. In these instances, we assess "strength" via the magnitude of the $W_{\rm diff}$ or outflow EW measurements for the sample. As shown above, $W_{\rm diff}$ and outflow EW values have a nonlinear but strong dependence on outflow velocities and line widths, and are somewhat sensitive to outflow columns and C_f as well (Rupke et al. 2005a). Larger outflow EW (or "stronger" outflows) may be produced by larger b_D, larger outflow velocities, or larger C_f, or any combination thereof. It is because we do not have the S/N necessary to constrain these quantities independently that we resort to EW measurements to quantify the physical characteristics of the outflows in our sample. The modeling described in this section relies on a very simplistic parameterization of the Mg II absorption profiles in our co-added spectra; however, it suggests that we are sensitive to saturated Mg II-absorbing outflows with velocities $\gtrsim$100 km s^{-1} in co-adds with S/N $\sim$ 6–9 pixel^{-1}. We will refer to this type of outflow as "strong" in later text. We are sensitive to outflows in S/N $\sim$ 3 pixel^{-1} co-adds only with large velocities and b_D. These findings will be discussed further in Section 8.

4.4. Mg II in Emission

We observe emission in the Mg II transition in both individual galaxies (see the P-Cygni profile in Figure 3) and in co-added spectra (e.g., Figure 5). Emission in the latter is obvious after the decomposition of systemic and outflow profiles is performed and one can identify the decrement of absorption on the red side of the 2796 Å line as compared to the red side of the 2803 Å transition. This emission is observed in $z \sim 1.4$ star-forming galaxies (W09), a luminous starburst galaxy at $z \sim 0.7$ (Rubin et al. 2010), as well as in narrow-line Seyfert galaxies such as two of the ultraluminous infrared galaxies (ULIRGs) studied in Martin & Bouché (2009). A similar P-Cygni-like profile in the Na I transition was observed in NGC 1808, a starburst galaxy driving an outflow (Phillips 1993). While the origin of this emission remains unclear, we suggest it may be at least in part due to resonance-line scattering off of the receding side of an expanding shell related to the observed outflow, as in the case of Lyα emission in LBGs (Pettini et al. 2001; K. H. R. Rubin et al. 2010, in preparation).

To better understand the effect of this emission on our outflow EW measurements, we develop an alternative method of characterizing the Mg II doublet profiles in co-added spectra. We again assume that the absorption at systemic velocity produces a saturated Gaussian absorption profile as in Section 4.2. We then further assume that there is additional emission on top of this continuum on the red side of each line with a Gaussian profile. The amplitudes of the emission lines have a ratio of either 2:1 or 1:1, appropriate for optically thin outflows and completely saturated outflow absorption, respectively (Lamers & Cassinelli 1999). The lines have a variable velocity offset with respect to systemic. In a true P-Cygni profile, the velocity at the peak of the emission (and the shape of the profile in general) depends on a number of factors, e.g., the outflow geometry and C_f, and the velocity dispersion of the outflowing gas. Our model can be written as follows:

$$F_{\rm obs}(\lambda) = C(\lambda)(1 - A_{\rm sym}(\lambda))(1 - A_{\rm flow}(\lambda)) + F_{\rm em}(\lambda), \quad (6)$$

$$F_{\rm em}(\lambda) = A_{2796} G(v - v_0, \lambda_{2796}, \sigma) + A_{2803} G(v - v_0, \lambda_{2803}, \sigma), \quad (7)$$

where $F_{\rm em}(\lambda)$ is emission in excess of the continuum and $A_{2796} = A_{2803}$ or $2A_{2803}$. We then fit this model to the red sides of *both* lines in the doublet simultaneously (where $A_{\rm flow} = 0$), in the velocity ranges 0 km s^{-1} $< v <$ 268 km s^{-1} and 0 km s^{-1} $< v <$ 1600 km s^{-1} for the 2796 Å and 2803 Å line, respectively. We subtract the fitted emission model ($F_{\rm em}(\lambda)$) from the co-add, divide out the model symmetric absorption, and measure the total boxcar EW in the range -1132 km s^{-1} $< v < 0$ km s^{-1} with respect to the 2796 Å line and in the range -384 km s^{-1} $< v < 0$ km s^{-1} with respect to the 2803 Å line in the resulting profile.

Because of the large number of free parameters in this model (5), this method does not generally produce acceptable fits for the co-added spectra in our study, as the results are often driven by noise features in the line profiles. However, the model does successfully characterize the red sides of the doublet lines in the much higher-S/N co-adds of W09. We find that in the W09 co-add with the strongest emission features (i.e., the lowest-M_* subsample), the line profile is fit well by the "optically thin" model with a 2:1 emission line ratio, and the calculated outflow EW is $\sim$11% lower than the outflow EW calculated with our standard procedure (described above in Section 4.2 and listed in Table 2). The co-add for the middle-M_* subsample is fit well by both optically thin and saturated models, and the corresponding outflow EWs are 18% lower and 8% higher, respectively, than the outflow EW calculated using the standard procedure. In co-adds such as the high-M_* W09 subsample, the difference in outflow EWs calculated with the two methods is <4%. While this model is quite simplistic, these results indicate that Mg II emission can cause either an under- or overestimate of the outflow EW when it is calculated using our standard method (Section 4.2). A more complete, physically motivated model including radiative transfer is required to fully quantify this effect, and additionally may more tightly constrain other characteristics (e.g., radial extent, density) of the cool gas outflow.

5. PROPERTIES OF THE SAMPLE GALAXIES

We wish to characterize outflow absorption strength at $0.7 < z < 1.5$ in galaxies with a range in SFR, M_*, and $\Sigma_{\rm SFR}$, as well as explore the evolution of outflows. To do this, we create subsamples of the galaxies with similar SFRs, M_*s, etc., and co-add spectra within a given subsample. We then compare outflow properties among these co-adds. Here we describe how luminosities, colors, sizes, M_*, SFR, and quantitative morphologies are measured for our sample.

5.1. Rest-frame Colors and Luminosities

We use rest-frame colors and luminosities from Weiner et al. (2006), which were derived from ACS imaging (Giavalisco et al. 2004) and Capak et al. (2004) ground-based photometry and converted to absolute M_B and rest-frame $U - B$ color using the K-correction routine of Willmer et al. (2006). Errors in the observed optical magnitudes and colors are 0.05–0.07 mag and 0.07–0.1 mag, respectively. The 1σ errors introduced by the K-correction procedure are 0.12 for M_B and 0.09 in $U - B$ (Weiner et al. 2006). The left-hand side of Figure 8 shows a color–magnitude diagram (CMD) for our sample. The solid line is from Willmer et al. (2006), and marks the division between the red sequence, or the narrow region populated by early-type E/S0s in the CMD, and the blue cloud, or the wider area in the CMD populated by bluer spirals and separated from the

Table 2
EW Measurements of Co-added Spectra

Subsample	S/N (pixel^{-1})	$W_{\rm diff}$[a] (Å)	Outflow EW[a] (Å)	EW(2796)[b] (Å)	EW(2803)[b] (Å)	Doublet Ratio
All	9.72	0.38 ± 0.11	**1.13 ± 0.17**	0.51 ± 0.05	0.47 ± 0.05	1.09 ± 0.16
$\log {\rm SFR_{UV}} < 0.555$	2.32	<0.94	<1.90	<0.44	<0.60	...
$0.555 < \log {\rm SFR_{UV}} < 0.942$	6.49	0.30 ± 0.17	1.01 ± 0.25	0.52 ± 0.08	0.40 ± 0.07	1.29 ± 0.30
$\log {\rm SFR_{UV}} > 0.942$	8.26	**1.10 ± 0.13**	**2.60 ± 0.21**	0.78 ± 0.06	0.65 ± 0.06	1.19 ± 0.14
"DEEP2-like"; high $\rm SFR_{UV}$	6.87	**1.46 ± 0.16**	**3.78 ± 0.22**	0.81 ± 0.07	0.80 ± 0.07	1.01 ± 0.12
$\log M_* < 9.86$	3.15	0.42 ± 0.35	**2.15 ± 0.47**	0.30 ± 0.15	0.11 ± 0.15	<11.35
$9.86 < \log {\rm M_*} < 10.49$	6.07	0.20 ± 0.18	0.81 ± 0.27	0.44 ± 0.08	0.48 ± 0.08	0.91 ± 0.22
$\log {\rm M_*} > 10.49$	8.04	**1.05 ± 0.14**	**2.69 ± 0.22**	0.81 ± 0.06	0.63 ± 0.06	1.28 ± 0.16
Early type	1.90	<1.17	<1.79	<0.70	0.58 ± 0.24	...
Merger candidate	4.60	0.47 ± 0.24	**1.37 ± 0.37**	0.77 ± 0.11	0.69 ± 0.11	1.10 ± 0.23
Late type	6.75	0.33 ± 0.16	**1.57 ± 0.24**	0.49 ± 0.07	0.56 ± 0.07	0.88 ± 0.17
$\log \Sigma_{\rm SFR} < -1.36$	3.44	0.77 ± 0.31	**2.07 ± 0.46**	0.42 ± 0.15	0.34 ± 0.13	1.21 ± 0.63
$-1.36 < \log \Sigma_{\rm SFR} < -0.66$	6.83	0.32 ± 0.16	1.16 ± 0.24	0.56 ± 0.07	0.41 ± 0.07	1.37 ± 0.29
$\log \Sigma_{\rm SFR} > -0.66$	6.80	**0.84 ± 0.16**	**1.83 ± 0.24**	0.61 ± 0.07	0.63 ± 0.07	0.97 ± 0.16
$\log \Sigma_{\rm SFR,Corrected} < -1$	4.65	0.64 ± 0.24	1.60 ± 0.35	0.44 ± 0.11	0.27 ± 0.10	1.64 ± 0.73
W09: $\log {\rm SFR_{UV}} < 1.15$	7.81	**1.43 ± 0.14**	**2.98 ± 0.17**	0.54 ± 0.06	0.53 ± 0.06	1.03 ± 0.16
W09: $1.15 < \log {\rm SFR_{UV}} < 1.45$	11.89	**1.05 ± 0.09**	**2.61 ± 0.14**	0.59 ± 0.04	0.55 ± 0.04	1.07 ± 0.11
W09: $\log {\rm SFR_{UV}} > 1.45$	13.46	**1.14 ± 0.08**	**2.98 ± 0.12**	0.70 ± 0.03	0.66 ± 0.04	1.06 ± 0.08
W09: $\log {\rm M_*} < 9.88$	8.31	**1.10 ± 0.13**	**2.57 ± 0.19**	0.53 ± 0.06	0.51 ± 0.06	1.03 ± 0.16
W09: $9.88 < \log {\rm M_*} < 10.45$	13.12	**1.22 ± 0.08**	**2.81 ± 0.12**	0.62 ± 0.04	0.60 ± 0.04	1.03 ± 0.09
W09: $\log {\rm M_*} > 10.45$	11.49	**1.17 ± 0.09**	**2.96 ± 0.14**	0.70 ± 0.04	0.61 ± 0.04	1.14 ± 0.10

Notes. Upper limits are given at the 2σ level. No doublet ratio is reported if either of the EW measurements is an upper limit. Rows beginning "W09" give measurements for co-adds from that work, with outflow EWs adjusted to include the EW in the outflowing absorption profile in the 2803 Å transition.

[a] Values in bold indicate statistically significant detections of outflow in the context of the simulations discussed in Section 4.3.

[b] Measured in the interval -384 km s^{-1} $< v < -200$ km s^{-1} relative to the systemic velocity of each transition.

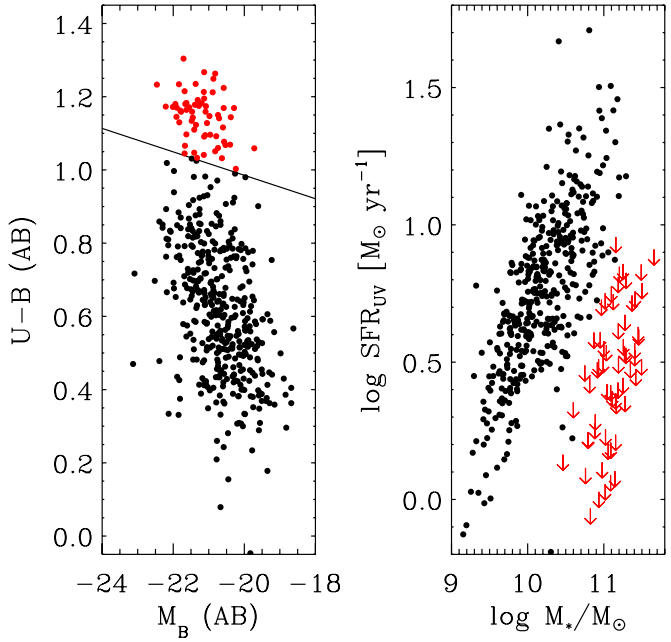

Figure 8. Left: CMD for all objects in our sample. The solid line marks the division between the red sequence and the blue cloud objects (in red and black, respectively); it is taken from Willmer et al. (2006). Right: $\rm SFR_{UV}$ vs. M_* for the full sample. Downward red arrows mark upper limits on the $\rm SFR_{UV}$ for objects on the red sequence.

(A color version of this figure is available in the online journal.)

red sequence by a narrow "valley" in the surface density of objects.

5.2. Sizes

We wish to measure $\Sigma_{\rm SFR}$ for our sample, where $\Sigma_{\rm SFR} = {\rm SFR}/\pi R^2_{\rm SF,1/2}$, for comparison with the suggested local threshold for driving outflows, $\Sigma_{\rm SFR} \gtrsim 0.1\ M_\odot\ {\rm yr^{-1}\ kpc^{-2}}$. In the local universe, measurements of the SFR from Hα, far-IR, or extinction-corrected UV fluxes are combined with measurements of the sizes of star-forming regions ($R_{\rm SF,1/2}$) to determine $\Sigma_{\rm SFR}$ (e.g., Meurer et al. 1997; Lehnert & Heckman 1995). The sizes are constrained using measurements of the half-light radius from Hα or UV (e.g., 2200 Å) imaging, which directly traces nebular emission or emission from young stars. Local starburst galaxies with high SFR per unit star-forming surface area (several $M_\odot\ {\rm yr^{-1}\ kpc^{-2}}$) have values of disk-averaged SFR surface density, or SFR per unit surface area in the optical disk ($\rm SFR/\pi D^2_{25}$),[8] which are at least 3 orders of magnitude lower (Martin 1999). It is therefore important to probe the spatial extent of UV flux when making size measurements of distant galaxies for comparison with local results. Continuum emission at redder wavelengths arises from older stellar populations, which are not expected to contribute to the driving of large-scale outflows.

We use the half-light radii of the TKRS galaxies measured by Melbourne et al. (2007) to parameterize galaxy size. These authors fitted successively larger elliptical apertures to the ACS images for each galaxy and calculated the fluxes and intensities within each aperture. An iterative curve-of-growth analysis was used to determine the flux level of the sky. From these measurements, the total flux of the object was calculated.

[8] D_{25} is the apparent isophotal diameter measured at surface brightness $\mu_{\rm B} = 25$ mag/arcsec^2.

Apparent half-light radii are equal to the semimajor axis of the ellipse that contained half of the total flux and were corrected for the point-spread function of the image. To determine half-light radii at 2200 Å in the restframe, we interpolate between the radii measured in the passbands to the red and blue of 2200 Å in the restframe of each object, assuming that all of the light measured in each band is observed at the central wavelength of the filter (4297 Å for the B_{435} band and 5907 Å for the V_{606} band). In cases in which 2200 Å is blueward of the rest-frame coverage of the B_{435}-band filter, we simply adopt the B_{435}-band radius. We then use the angular diameter distance to compute the rest-frame UV half-light radius in kiloparsecs ($R_{1/2}$). Melbourne et al. (2007) estimate that they obtain accurate radii to within <10%. This level of uncertainty applies strictly to the rest-frame B-band half-light radii they derive by combining the radii measured in the observed bands in a weighted mean, with weights dependent on the overlap of each observed passband with the rest-frame B band. We assume this level of uncertainty applies to our $R_{1/2}$ as well.

We choose to use $R_{1/2}$ to parameterize the sizes of the star-forming regions in our galaxies for its simplicity; however, this measure may in fact significantly overestimate the size scales relevant for driving outflows. Many of the galaxies have extended and clumpy morphologies, such that $R_{1/2}$ is quite large (>10 kpc), while much of the UV emission arises in a few small but widely separated bright knots. On the other hand, the distance between star-forming knots may be intimately connected to the morphology of the outflowing gas itself (see, e.g., Heckman et al. 1990, Martin 2006, for some discussion of outflow morphology). Future studies of outflows in individual galaxies will warrant more careful analysis of the size scale and distribution of star formation.

5.3. Stellar Mass

Near-IR photometry of the GOODS-N field was published by Bundy et al. (2005), who calculated M_* for 202 objects in our sample (out of a total of 468). As we did not wish to limit this study to objects with K-band derived M_*, we use a calibration given in W09 to convert rest-frame color and magnitudes into M_*. Bell et al. (2003) compute the relation between rest-frame color and M_*/L_B using SDSS and 2MASS photometry of local galaxies. They give this relation for a "diet Salpeter" initial mass function (IMF):

$$\log M_*/L_B(z=0) = -0.942 + 1.737(B-V)_{\rm Vega}.$$

This must be adjusted according to the redshift of each galaxy. W09 derived a redshift correction to this relation using the K-band magnitudes and M_* (calculated assuming a Chabrier IMF) available for 11,924 objects in the DEEP2 redshift survey (Davis et al. 2003; Bundy et al. 2006). These objects lie in a redshift range $0 < z < 1.5$. W09 performed a least-squares fit between M_* derived from rest-frame color and M_* derived using K-band photometry, and give a correction term C_K:

$$M_* = L_{B,\rm Vega} \times M_*/L_B(z=0) C_K(U-B, z),$$
$$\log C_K(U-B, z) = -0.0244 - 0.398z + 0.105(U-B)_{\rm Vega}.$$

The authors report a scatter of 0.25 dex about the fit for C_K. We apply this correction to our data and compare K-band M_* to the corrected color-derived masses where possible (for 202 objects). We find that there is a 0.09 dex mean offset and a dispersion of 0.22 dex between the two M_* estimates. We use the corrected color-derived masses with a Chabrier IMF for the full sample in the following analysis.

5.4. Star Formation Rate

The rich multi-wavelength data set in the GOODS-N field makes several different methods available for estimating the total SFRs for the galaxies in our sample. [O II] line luminosities have been measured for TKRS galaxies (Weiner et al. 2006). 24 μm fluxes and IR-based SFRs for a subset of objects in our sample are available from Melbourne et al. (2005). In order to make comparisons with W09, we adopt their method of determining SFR. The BV photometry of Capak et al. (2004) measures the flux at 1800–2800 Å and 2200–3400 Å in the restframe for our redshift range. We use these measurements to derive absolute magnitudes at 1500 Å and 2200 Å using the K-correction code described in Willmer et al. (2006) and Weiner et al. (2005). Using these luminosities we find the slope of the UV continuum, β, and calculate the attenuation from this slope using the relation $A_{\rm FUV} = 3.16 + 1.69\beta$ (Seibert et al. 2005; Treyer et al. 2007). There is a $\pm$0.9 mag scatter in this relation, which results in a 0.36 dex uncertainty in the SFRs. We use the values of $A_{\rm FUV}$ to calculate an unextincted UV luminosity and in turn calculate the SFR (Kennicutt 1998) assuming a Kroupa IMF:

$$\mathrm{SFR_{UV}}(M_\odot\ \mathrm{yr}^{-1}) = 1.0 \times 10^{-28}\ L_{1500\text{Å}}\ (\mathrm{erg\ s^{-1}\ Hz^{-1}}).$$

To investigate systematic errors in these SFR estimates, we compare them to SFRs derived from the IR luminosities of Melbourne et al. (2005). These authors used the publicly available MIPS imaging of the GOODS-N field to measure 24 μm fluxes to a limit of 25 μJy, and used the Le Floc'h et al. (2005) prescription to convert 24 μm flux to total IR luminosity ($L_{\rm IR}$). 213 of the 407 blue cloud galaxies in our sample have $L_{\rm IR}$ estimates available. We use the Bell et al. (2005) relation between $L_{\rm IR}$ and SFR with a Kroupa IMF to calculate SFR(IR) for these galaxies, ignoring the contribution to the SFR probed by unextincted light from young stars in the UV, which we expect to be small (Bell et al. 2005; W09). We find that for IR-selected galaxies, which may have slightly larger IR-to-UV emission ratios than is typical (W09), $L_{\rm IR}$-derived SFRs are 0.21 dex higher on average than the UV-derived SFRs, with a dispersion in the offset between IR- and UV-based SFRs of 0.43 dex. This offset is likely smaller for galaxies not detected in the MIPS imaging. For consistency with W09, and because we lack $L_{\rm IR}$ measurements for nearly half of the blue cloud galaxies in our sample, we adopt the UV-derived SFRs described above in our analysis. However, uncertainties in these estimates must be considered when absolute SFRs are discussed, as in Section 6.2. Bell et al. (2005) report systematic and random errors in their IR/UV-derived SFRs of 0.3 and 0.4 dex; we must consider these errors in addition to those introduced from using purely UV-derived SFRs.

The right-hand side of Figure 8 shows a plot of $\log \mathrm{SFR_{UV}}$ versus $\log M_*$ for all objects in our sample. Upper limits on the SFRs in red sequence galaxies are marked in red. While our sample includes galaxies in a range of M_* comparable to the sample of W09, the mean SFR in the W09 sample is ~0.57 dex higher than in the present sample.

5.5. Morphology

We use the Gini (G) and M_{20} measurements made for TKRS galaxies in the i_{775} band by J. Lotz (2008, private communication) to quantify galaxy morphology. These are nonparametric measurements described in Lotz et al. (2004, 2006). G quantifies the relative distribution of light among

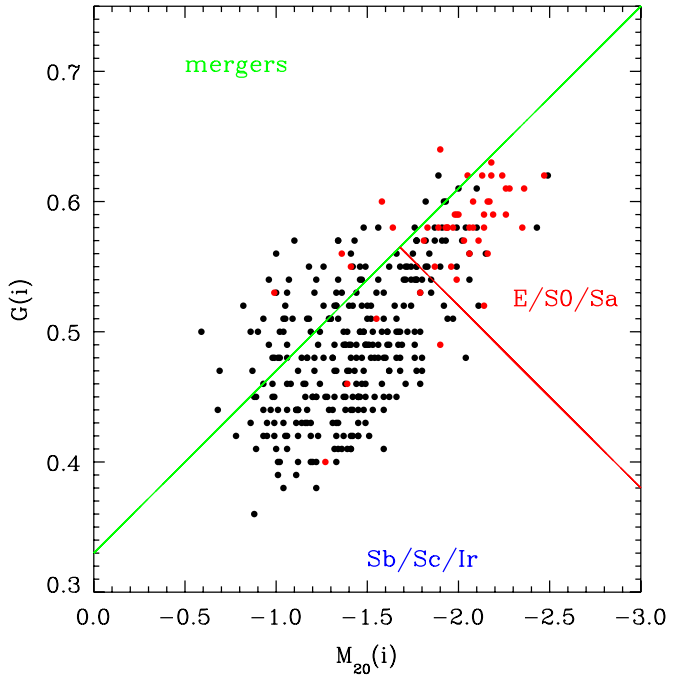

Figure 9. G vs. M_{20} measured in the i_{775} band for objects in our sample. Measurements were provided by J. Lotz (2008, private communication). The colored lines show the regions occupied by different morphological types and are adopted from Lotz et al. (2008). Red sequence galaxies are marked in red.

(A color version of this figure is available in the online journal.)

a galaxy's pixels, and is high if there are only a few very bright pixels in the galaxy image. M_{20} is the second-order moment of the brightest 20% of a galaxy's pixels; it is larger for galaxies in which the brightest pixels are farther from each other. Figure 9 shows the distribution of these parameters for our sample (excluding 115 objects which lack high-quality G/M_{20} measurements). The lines separating different morphological types shown in the figure are taken from Lotz et al. (2008), who found that these divisions are appropriate for galaxies at $0.2 < z < 1.2$. There are 63 mergers, 226 late-type objects, and 64 early-type objects with robust G/M_{20} measurements in our sample.

6. DIVISION OF SAMPLE BY GALAXY PROPERTIES

6.1. Division by $\mathrm{SFR_{UV}}$, M_*, *and Morphology*

To examine trends in $W_{\rm diff}$ (where $W_{\rm diff} = W_{2796\ \text{Å,blue}} - W_{2803\ \text{Å, red}}$) and outflow EW with $\mathrm{SFR_{UV}}$, M_*, and morphology, we divide our spectra into several different subsamples and co-add them. We calculate $W_{\rm diff}$ and outflow EW for each subsample. These subsamples and measurements, as well as corresponding measurements for co-adds presented in W09, are listed in Table 2.

First, we co-add galaxies on the red sequence. The co-add has a very low $\mathrm{S/N} = 1.4$ pixel^{-1} in the continuum surrounding Mg II, and so cannot be used to examine outflows in these objects. Because of their low S/N, we exclude all red sequence galaxy spectra from the subsamples described in the following, with the exception of the morphologically divided subsamples.

We choose to divide the TKRS galaxies by the 25th and 75th-percentile values of $\log \mathrm{SFR}$ (0.555, 0.942) and $\log M_*$ (9.86, 10.49). Co-adds of the spectra for these subsamples are shown in Figure 10. Figure 11 shows $W_{\rm diff}$ for the $\mathrm{SFR_{UV}}$-divided and M_*-divided subsamples in gray. Values for $W_{\rm diff}$ are shown as diamonds if they represent significant detections of outflows in the context of the simulations discussed in Section 4.3; i.e., in co-adds with $\mathrm{S/N} \sim 3$ pixel^{-1}, detections are significant if $W_{\rm diff} \gtrsim 0.8$ Å, whereas in co-adds with $\mathrm{S/N} \sim 6$ or 9 pixel^{-1}, significant detections have $W_{\rm diff} > 0.5$ or >0.4 Å. Detections which are not significant are shown as upper limits. The outflow absorption strength (as quantified by $W_{\rm diff}$) rises significantly with $\mathrm{SFR_{UV}}$ and M_* between the middle and high-

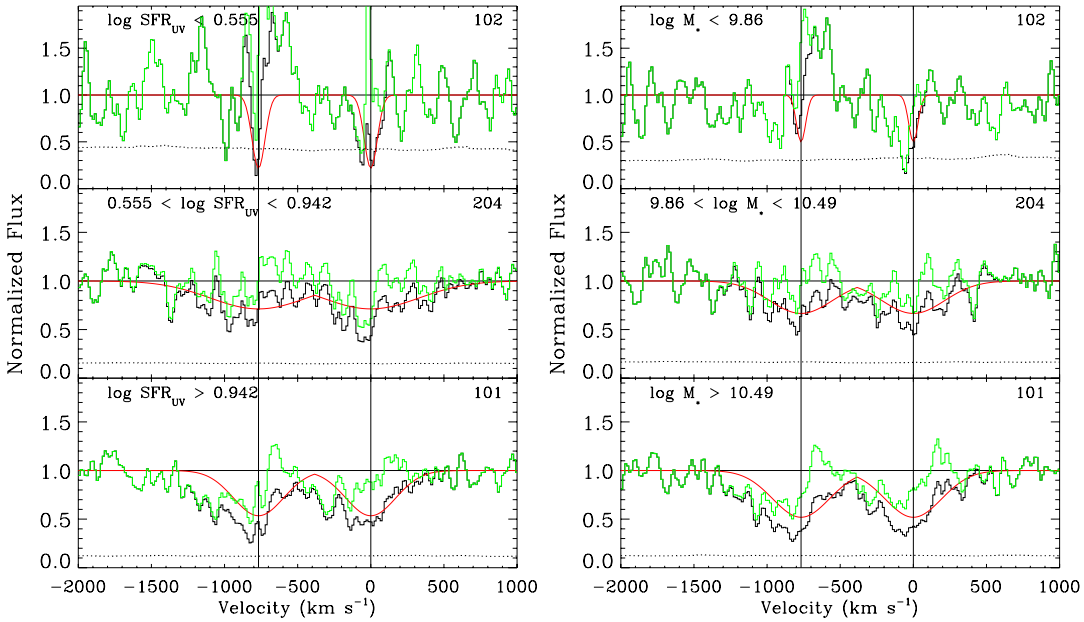

Figure 10. Sections of the co-added spectra for subsamples divided by $\mathrm{SFR_{UV}}$ (left) and M_* (right) around Mg II (black). The co-adds have been normalized to the level of the continuum surrounding the absorption lines as described in the text. The symmetric absorption profile is shown in red; the outflow profile is shown in green. The error in each pixel is shown with the dotted lines and the black vertical lines mark the systemic velocity for each transition. The number of spectra in each subsample is shown in the upper right of each panel.

(A color version of this figure is available in the online journal.)

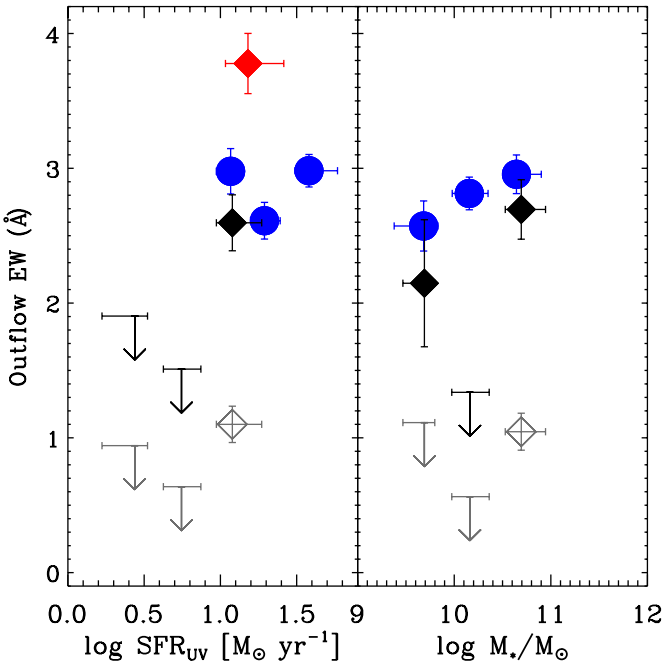

Figure 11. Comparison between the outflow absorption strength, SFR_{UV} (left), and M_* (right). Each point corresponds to a single co-add. Gray open diamonds and arrows plot W_{diff} measurements for the TKRS subsamples divided by the 25th and 75th percentile values of SFR_{UV} and M_*. Black diamonds and arrows show the outflow EW results from the decomposition procedure for the same subsamples. The red diamond shows the outflow EW (from the decomposition procedure) for the "DEEP2-like" subsample selected by M_* and SFR_{UV} (see Section 6.3). Blue circles show results from W09. 2σ upper limits are shown when the error on the outflow absorption measurement (W_{diff} or outflow EW) is twice the central value, or when the measured W_{diff} or outflow EW does not yield a significant detection of outflows as indicated by the simulations discussed in Section 4.3. See Section 6 for further details.

(A color version of this figure is available in the online journal.)

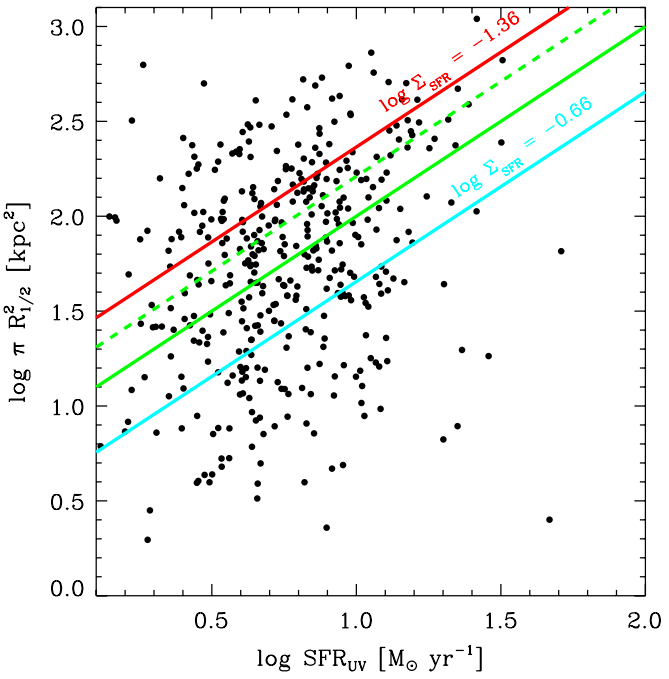

Figure 12. $\log \pi R^2_{1/2}$ vs. $\log SFR_{UV}$ for the blue galaxies in the TKRS sample. Lines show our subdivisions in $\log \Sigma_{SFR}$. All galaxies with $\log \Sigma_{SFR} \leqslant -1.36$ are above the red line; galaxies with $-1.36 < \log \Sigma_{SFR} \leqslant -0.66$ are between the red and cyan lines; galaxies with $\log \Sigma_{SFR} > -0.66$ are below the cyan line. A line of constant $\log \Sigma_{SFR} = -1$ is shown in solid green. The dashed green line indicates where galaxies in the sample lie with respect to a line of constant $\log \Sigma_{SFR} = -1$ when the SFRs are increased by 0.21 dex.

(A color version of this figure is available in the online journal.)

est SFR_{UV} and M_* subsamples. We also perform our decomposition analysis on each of these co-adds, shown in Figure 10. Measurements of outflow EW for each co-add are shown in Figure 11 (black) and show consistency with the W_{diff} measurements. Again, outflow EW values are shown as diamonds if they represent significant detections of outflows: at low S/N, an outflow EW $\gtrsim 1.8$ Å is significant, while at S/N ~ 6 or 9 pixel^{-1}, outflow EWs > 1.2 Å or >1.0 Å are significant. All other measurements are shown as upper limits. Outflow EW results from W09, adjusted to include the outflow EW measured in the 2803 Å transition, are shown in blue. The high outflow EW for the lowest-M_* TKRS subsample suggests the detection of outflows; however, this co-add has S/N ~ 3 pixel^{-1}, and the corresponding W_{diff} measurement does not yield a significant outflow detection. Due to the inconsistency between the two measurements of outflow absorption strength, we consider this detection tentative. Note that measurements of outflow absorption strength are significantly higher for the W09 $z \sim 1.4$ galaxies than for the middle-M_* TKRS galaxies. As discussed in Section 5.4, while the TKRS and W09 galaxies have a similar range in M_*, on the whole the TKRS galaxies have a mean SFR_{UV} that is lower by $\sim$0.6 dex. In addition, the highest-M_* TKRS galaxies include objects with the highest SFRs in the sample. This suggests that either outflow absorption strength is most closely correlated with SFR, or that there is evolution of outflows in $\log M_* \sim 10$ galaxies between $z \sim 1.4$ and 1. This will be discussed in more detail in Section 8.

The co-add of early-type galaxies (as classified by the G–M_{20} analysis) has very low S/N and is not useful for measuring outflow absorption. W_{diff} and outflow EW for the merger candidate and late-type subsamples are the same within the errors, at $W_{diff} \sim 0.3$–0.5 Å and outflow EW $\sim$1.4–1.6 Å; i.e., there does not appear to be a significant difference in the strength of absorption due to outflows in late-type galaxies and merger candidates (see Table 2). However, it is difficult to disentangle the effects of morphology and SFR_{UV} on outflow strength in this analysis. Studies of galaxy mergers (i.e., LIRGs and ULIRGs) in the local universe show that they host exceptionally strong outflows (Martin 2005; Rupke et al. 2005b) in comparison to local late-type galaxies. On the other hand, these merger remnants also have some of the highest SFRs at $z \sim 0$. This degeneracy between morphology and SFR is broken at $z \sim 1$, where the majority of LIRGs have disk-like morphologies (Melbourne et al. 2008); thus, galaxies at $z \sim 1$ may provide the ideal laboratory for investigating the effects of these two parameters on outflows. Higher S/N spectra are required to examine these effects in greater detail.

6.2. Division by Σ_{SFR}

To test for a dependence of outflow strength on SFR surface density (Σ_{SFR}) in our sample, we assume that $R_{SF,1/2} = R_{1/2}$, and combine this with our measure of SFR_{UV} to calculate the global (i.e., flux averaged) $\Sigma_{SFR} = SFR/\pi R^2_{SF,1/2}$ for each object. Figure 12 shows the distribution of $\log SFR_{UV}$ and $\log \pi R^2_{1/2}$ for the blue galaxies in the TKRS sample. The red and cyan lines mark the 25th and 75th percentile values of $\log \Sigma_{SFR}$ (-1.36, -0.66), which we use to subdivide the sample. Figure 13 shows

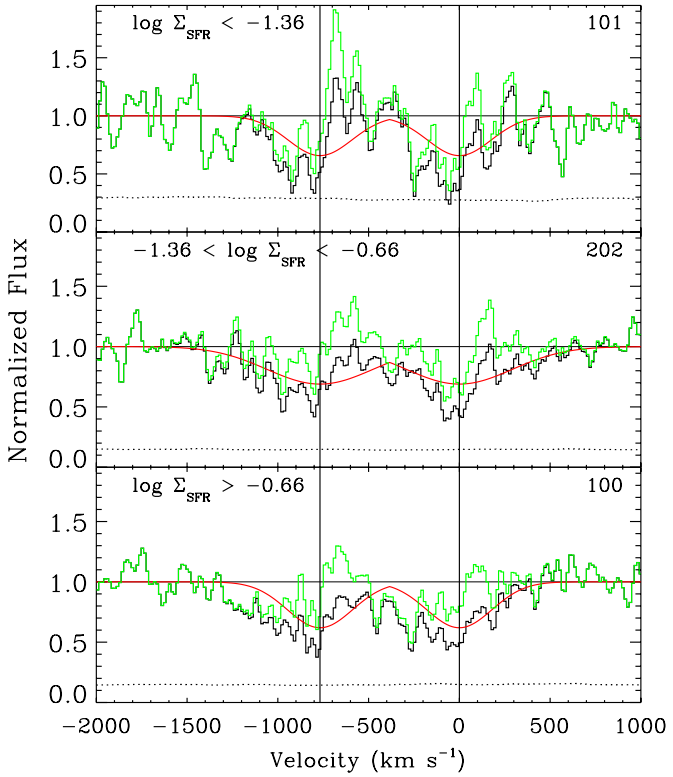

Figure 13. Sections of the co-added spectra for subsamples divided by Σ_{SFR} around Mg II (black). The co-adds have been normalized to the level of the continuum surrounding the absorption lines as described in the text. Colored lines are the same as in Figure 10. The number of spectra in each subsample is shown in the upper right of each panel.

(A color version of this figure is available in the online journal.)

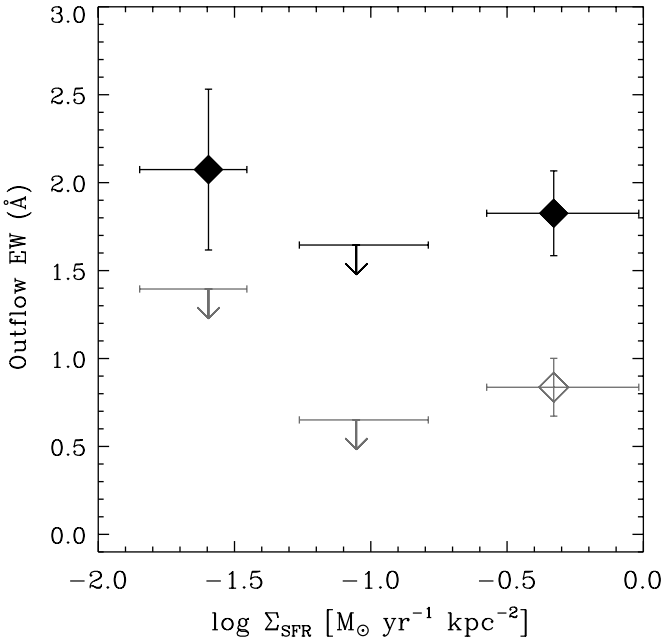

Figure 14. Outflow absorption strength vs. Σ_{SFR}. Gray open points plot W_{diff} measurements for the subsamples divided by the 25th and 75th percentile values of Σ_{SFR}. Black points show the outflow EW results from the decomposition procedure for the same subsamples. 2σ upper limits are shown when the error on the outflow absorption measurement (W_{diff} or outflow EW) is twice the central value, or when the measured W_{diff} or outflow EW does not yield a significant detection of outflows as indicated by the simulations discussed in Section 4.3. See Section 6 for further details.

the co-adds of the spectra in these subsamples and the results of the decomposition procedure.

Figure 14 shows W_{diff} and outflow EW versus Σ_{SFR} for these co-adds. As in Section 6.1, diamonds are plotted only in the case of a significant detection of outflows. There is a slight increase in outflow absorption strength with Σ_{SFR} evident between the middle- and high-Σ_{SFR} subsamples. The lowest-Σ_{SFR} subsample has S/N ~ 3 pixel^{-1}, and while it appears that the outflow EW yields a significant detection of outflows in this co-add, the W_{diff} measurement does not, and this inconsistency leads us to consider this detection tentative. Comparing Figures 11 and 14, we note that the outflow absorption strength is higher in the high-SFR_{UV} subsample than in the high-Σ_{SFR} subsample, indicating that galaxies with the highest SFRs in the sample drive stronger outflows than those with the highest Σ_{SFR}'s.

We also consider our results in the context of the suggested local "threshold" for driving outflows, $\Sigma_{SFR} \gtrsim 0.1\ M_\odot\ \mathrm{yr}^{-1}\ \mathrm{kpc}^{-2}$. Because the existence of and a precise value for a strict threshold Σ_{SFR} for driving outflows have not yet been observationally established (see, e.g., Strickland et al. 2004), it is interesting to search below the suggested threshold for evidence of winds. Given the uncertainty in our absolute SFR determinations, it is difficult to differentiate which of our individual galaxies have Σ_{SFR} above or below $\Sigma_{SFR} = 0.1\ M_\odot\ \mathrm{yr}^{-1}\ \mathrm{kpc}^{-2}$. The solid green line in Figure 12 shows a line of constant $\Sigma_{SFR} = 0.1\ M_\odot\ \mathrm{yr}^{-1}\ \mathrm{kpc}^{-2}$ for comparison with the distribution of our sample in $\pi R_{1/2}^2$–SFR_{UV} space. From the placement of this line, it appears that many of the galaxies in the middle-Σ_{SFR} subsample have Σ_{SFR} values below the threshold. If we shift this line by -0.21 dex in SFR_{UV} to reflect our possible systematic underestimate of SFR (see Section 5.4) as indicated by the dashed green line, a smaller fraction of the sample falls below the threshold. A 0.21 dex correction to the Σ_{SFR} values for the sample is likely too large, as this correction is derived from a comparison between IR- and UV-based SFRs for the IR-detected galaxies only. However, we apply this correction and create a new subsample with "corrected" $\Sigma_{SFR} < 0.1\ M_\odot\ \mathrm{yr}^{-1}\ \mathrm{kpc}^{-2}$. The co-add of these spectra (called the $\log \Sigma_{SFR,Corrected}$ sample in Table 2) yields S/N ~ 4.7 pixel^{-1}, $W_{diff} = 0.64 \pm 0.24$ Å, and outflow EW $= 1.60 \pm 0.35$ Å. These values represent, at best, marginally significant detections, as the S/N of this co-add falls mid-way between the lowest and middle S/N levels used in the simulations, and would be considered insignificant in the former regime but significant in the latter. This suggests, however, that some galaxies below a *flux-averaged* $\Sigma_{SFR} = 0.1\ M_\odot\ \mathrm{yr}^{-1}\ \mathrm{kpc}^{-2}$ drive outflows. Because there is a 1σ dispersion in the comparison between SFR_{UV} and SFR(IR) of 0.43 dex, some fraction of galaxies in this subsample do have true Σ_{SFR} values above the threshold; however, the absorption line profile in the co-added spectrum reflects the mean absorption properties of the subsample, which has a Σ_{SFR} below the threshold in the mean.

6.3. Redshift Dependence

As noted in Section 5.4, the TKRS and W09 samples span a similar range in M_*, but the TKRS sample is offset to lower SFRs by $\sim$0.6 dex. To examine evolution in outflow properties with redshift, we compare our outflow measurements to those from W09. The 25th and 75th percentile M_* divisions of our sample are quite close to the divisions used in W09 ($\log M_* < 9.88$, $9.88 < \log M_* < 10.45$, and $\log M_* > 10.45$). To further investigate similarities between the two sets of

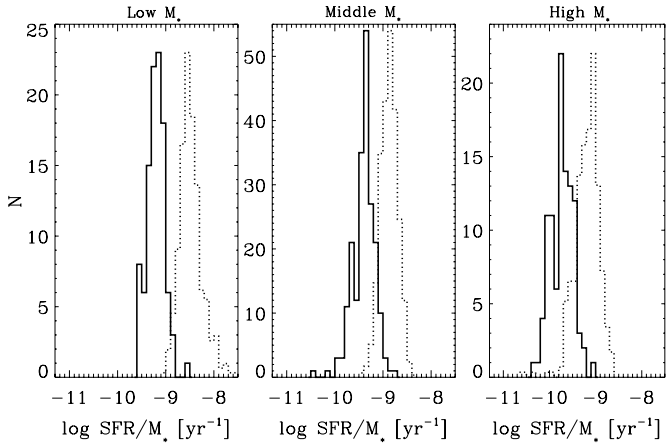

Figure 15. Normalized SSFR distributions for galaxies in the low-M_* (left), middle-M_* (middle), and high-M_* (right) subsamples. The solid histograms show the SSFR distributions for TKRS galaxies. The dotted histograms show the SSFR distributions for the W09 M_*-divided subsamples, normalized to have the same maximum values as the corresponding TKRS distributions.

subsamples, we compare the distributions of specific SFR (SFR/M_*; SSFR). Figure 15 shows the SSFR distribution of TKRS (solid line) and DEEP2 (dotted line) galaxies in each M_* bin. Each subsample has a symmetric distribution in SSFR at both redshifts; these distributions are offset from each other because of the decline in global SFR with decreasing redshift. The symmetry of the distributions suggests that none of the subsamples are severely contaminated with non-star-forming galaxies. See Section 8.4 and Figure 19 for further comparison of the SSFR–M_* relations for the W09 and TKRS samples and a discussion of the evolutionary connection between the galaxies at the two epochs.

Although the TKRS and W09 samples are nearly disjoint in $\mathrm{SFR_{UV}}$–M_* space, we may construct a comparison subsample of 43 TKRS galaxies which lie above the lower envelope of the SFRs for the W09 galaxies. Figure 16 shows the TKRS (black circles) sample and a random selection of half of the W09 (green crosses) sample in $\log \mathrm{SFR_{UV}} - \log M_*$ space. We include all TKRS galaxies above the solid line in a high-$\mathrm{SFR_{UV}}$, "DEEP2-like" sample. Figure 17 shows the co-add and decomposition analysis for this subsample.

The red point in Figure 11 shows results for this DEEP2-like sample. This sample, as well as the high-$\mathrm{SFR_{UV}}$ TKRS subsample, have outflow EWs similar to or larger than the W09 co-adds. This confirms our previous finding that galaxies at $z \sim 1.4$ and 1 with similarly high SFRs have strong outflow absorption. We note that the galaxies in the highest-M_* TKRS subsample have a median $\log \mathrm{SFR_{UV}} = 0.99$, with 68% of the subsample in the range $0.78 < \log \mathrm{SFR_{UV}} < 1.22$. These galaxies therefore have $\mathrm{SFR_{UV}}$ values in a range similar to the W09 sample, and the high outflow EW for this subsample is consistent with the measurements for our other high-$\mathrm{SFR_{UV}}$ subsamples.

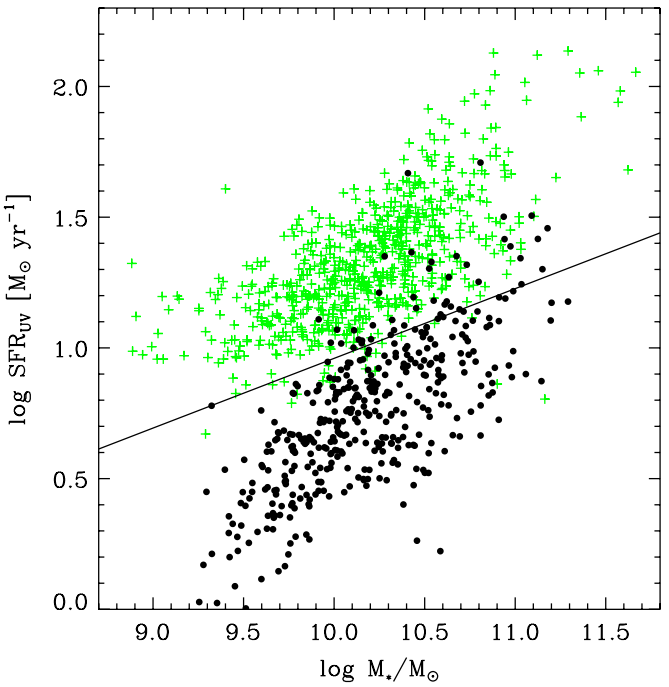

Figure 16. $\log \mathrm{SFR_{UV}}$ vs. $\log M_*$ for the full TKRS sample (in black) and a randomly selected portion of the DEEP2 sample (in green) from W09. The line shows the cut applied to the TKRS sample for the purposes of selecting TKRS galaxies with $\mathrm{SFR_{UV}}$'s similar to the $\mathrm{SFR_{UV}}$ values in the W09 sample.

(A color version of this figure is available in the online journal.)

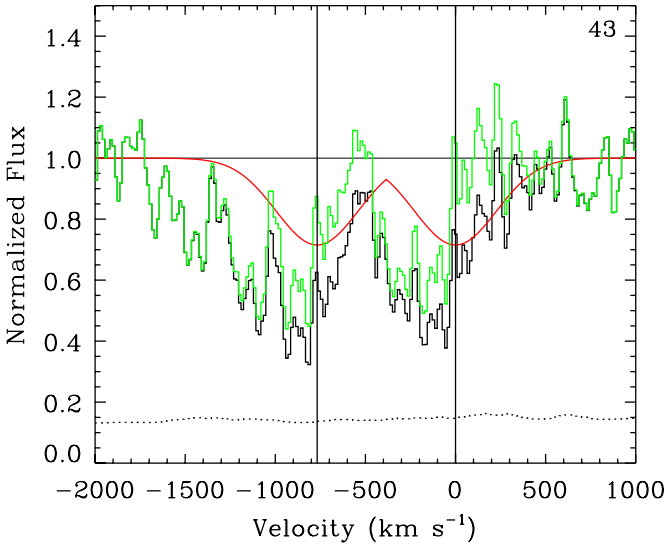

Figure 17. Sections of the high-SFR "DEEP2-like" sample co-add around Mg II. The co-add has been normalized to the level of the continuum surrounding the absorption lines as described in the text. The colored lines are the same as in Figure 10. The number of spectra in the sample is shown in the upper right.

(A color version of this figure is available in the online journal.)

7. Fe II 2586, 2600 ABSORPTION

We now focus on measurements of Fe II absorption in our spectra. A constraint on the extent to which Fe II 2586, 2600 absorption is detected with Mg II in outflowing gas is valuable for a number of reasons, as discussed in Martin & Bouché (2009). While Mg II is found over a wide range of ionization parameter (or number of ionizing photons per atom), Fe II is present only at lower ionization parameters (e.g., in higher-density gas), and so may provide information about outflow gas density (e.g., Narayanan et al. 2008). Second, the Fe II 2586, 2600 transitions have oscillator strengths 0.11 and 0.39 times that of Mg II 2796, and Fe is less abundant in general than Mg; thus, Fe II absorption lines are generally less strongly saturated than Mg II lines. They may therefore be used to place more stringent constraints on the cool outflow column density. For instance, Martin & Bouché (2009) find that the Fe II absorption tracing ULIRG outflows at $z \sim 0.25$ requires optical depths

2–3 times larger than those derived from analysis of Mg II. Finally, because Mg is generated in Type II supernovae (i.e., in younger stellar populations than Fe), comparison of the relative abundances of Mg II and Fe II in the outflow may constrain the enrichment history of the gas.

The Fe II 2600 transition is always weaker than Mg II 2796 in QSO absorption line systems, with at most two-third of the EW of Mg II 2796 (Churchill et al. 2000). In stellar atmospheres, Fe II 2600 reaches its maximum absorption strength in F9–G2 stars (similar to Mg II, which reaches its maximum strength in F8–G1 stars; Kinney et al. 1993, although *asymmetric* absorption is exhibited in B–F stars as mentioned in Section 4). In early-type stars, Fe II lines do not exhibit P-Cygni profiles or asymmetric absorption; instead, if mass-loss effects are observed the lines are simply blueshifted (Snow et al. 1994). Our analysis of these lines in UVBLUE theoretical stellar spectra (Rodríguez-Merino et al. 2005) shows that Fe II 2600 lines are also consistently weaker than Mg II 2796 in stellar spectra, as in QSO absorption line system spectra. To compare the EWs of these transitions, we first normalize the model spectra, calculating the continuum in the same regions used for our galaxy co-adds. We measure EWs between -500 km s^{-1} $< v <$ 500 km s^{-1} for Fe II 2600 and between -500 km s^{-1} $< v <$ 385 km s^{-1} for Mg II 2796. Note that these spectral regions contain absorption not only from the named transitions, but from several weaker transitions also exhibited by stellar atmospheres (the Fe II* 2599 transition, for example). Using solar metallicity models, we obtain EW(2796) $\sim$ 6.8 Å and EW(2600) $\sim$ 3.1 Å for a solar-type star, yielding a ratio of $\sim$2.2. As the atmospheres become hotter, the EWs of both ions decrease, although the EW(2600) value decreases much more strongly with increasing temperature than EW(2796).

We now measure Fe II EWs and analyze Fe II line profiles to constrain the origin of the Fe II absorption in our spectra.

7.1. Fe II Absorption in TKRS2158

As noted in Section 3.1, we observe blueshifted Fe II lines in the spectrum of TKRS2158. Velocity offsets are given in Table 1. Velocities are slightly inconsistent among the various Fe II transitions; this may be due to poorly subtracted sky emission, intrinsic Fe II* emission, or other sources of noise in the spectrum. In general, Fe II velocities are slightly lower than the offsets measured for Mg II. This may occur if Fe II absorption is weaker at the highest velocities, and/or if Mg II emission fills in the line profile near systemic velocity and effectively shifts the line center further to the blue. We conclude that Fe II traces outflowing gas in this object, although we cannot confirm that it traces gas in the same velocity range as Mg II.

7.2. Fe II Absorption in Co-added Spectra

To analyze Fe II absorption in our galaxy spectra, we create a new subsample, selecting objects with $z \gtrsim 0.8$ such that spectral coverage of Fe II λλ2586, 2600 is available, and further selecting objects with log SFR$_{\rm UV} \geqslant 1$, for a final subsample size of 66 objects. This latter cut selects objects with the bluest colors and the strongest continua near 2600 Å, which minimizes unphysical effects due to poorly determined sky levels. Co-adding spectra of fainter galaxies in the sample yields Fe II absorption with unphysical line profiles and thus these objects are excluded from this analysis.

Figure 18 shows Fe II and Mg II line profiles for this subsample. We note that the Fe II lines are slightly deeper than the Mg II lines in the co-add, in contrast to examples from QSO absorption line systems (Churchill et al. 2000) and stellar atmospheres. This inconsistency suggests that (1) the depth of Fe II is affected by unphysical artifacts resulting from poor sky subtraction even in this subsample of the brightest galaxies, (2) Fe II-absorbing gas has a larger C_f than Mg II, or (3) the Mg II absorption is being filled in by emission in the same transition.

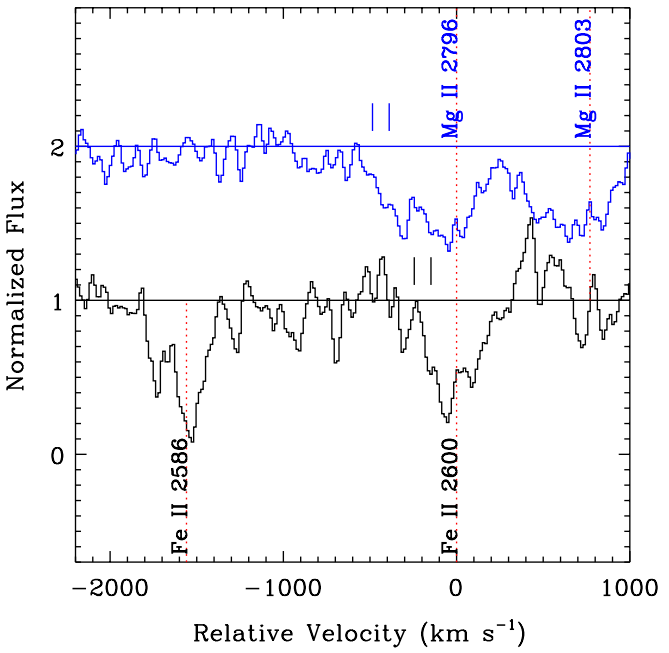

Figure 18. Sections of the co-add of galaxy spectra used in the Fe II analysis with log SFR$_{\rm UV} \geqslant 1$. The black spectrum shows the region surrounding Fe II 2586, 2600, and the blue spectrum shows the region surrounding Mg II 2796, 2803. Co-adds have been normalized to the level of the continuum surrounding the absorption transitions, indicated with the horizontal lines. The section surrounding Mg II has been offset by +1 in flux. The velocity for the black spectrum is measured relative to the rest velocity of the 2600 Å line; for the blue spectrum it is measured relative to the rest velocity of the 2796 Å line. Vertical red dotted lines show rest velocities of all lines of interest. Vertical blue and black marks indicate the velocities at which the absorption decreases to 80% and 60% of the continuum level for the Mg II 2796 and Fe II 2600 lines, respectively.

(A color version of this figure is available in the online journal.)

We measure the EW in the Fe II lines in the co-added spectrum between -300 km s^{-1} $< v <$ 300 km s^{-1}, as well as on the blue (-300 km s^{-1} $< v <$ 0 km s^{-1}) and red (0 km s^{-1} $< v <$ 300 km s^{-1}) sides of each. The total EWs for each line are approximately the same (EW(2586) $= 1.99 \pm 0.15$ Å and EW(2600) $= 1.86 \pm 0.15$ Å), indicating that Fe II is completely saturated in this co-add. The total EWs of the Mg II absorption lines in the same velocity range are significantly larger (EW(2796) $= 2.36 \pm 0.10$ Å), yielding EW(2796)/EW(2600) $\sim$ 1.2, a slightly smaller ratio than expected from analysis of stellar atmospheres and QSO absorption lines. This again may be due to emission filling in the Mg II absorption line profiles. We measure a larger EW on the blue side of the 2600 Å line than on the red side (EW(2600, blue) $= 1.12 \pm 0.11$ Å and EW(2600, red) $= 0.79 \pm 0.10$ Å). This in consistent with a scenario in which the Fe II-absorbing gas is outflowing. We find that the EW on the blue and red sides of the 2586 Å line in the co-add are the same within the errors (EW(2586, blue) $= 0.99 \pm 0.11$ Å and EW(2586, red) $= 1.10 \pm 0.11$ Å). We cannot conclude that Fe II-absorbing gas is outflowing from analysis of this line

alone; however, the symmetry of the profile does not rule out an outflow scenario. The oscillator strength of this transition may simply be too low for it to obviously trace blueshifted gas. In contrast, Martin & Bouché (2009) find that both the Fe II 2586 and 2600 Å lines are saturated and have similar line profiles in ULIRG spectra. See Section 8.1.2 for a discussion of the upper limit on N(H) in the outflow derived from Fe II EWs.

We also examine the relative velocity extent of the Fe II and Mg II absorption lines. In Figure 18, the Mg II 2796 absorption appears to extend to larger velocities than the Fe II 2600 absorption, although it may be that high-velocity Fe II absorption is hidden in the noisy continuum of the co-add. Further, the Mg II 2796 line has a high velocity tail which decreases in strength gradually with increasing velocity offset, whereas the Fe II 2600 line does not exhibit a gradually decreasing "tail" of absorption to high velocities. If the Fe II absorbing gas is indeed outflowing, this suggests that the majority of the gas does not attain velocities as high as those attained by the Mg II absorbing gas, although we again caution that we are likely not sensitive to absorption at the highest velocities probed by either ion (Martin & Bouché 2009).

To quantify the differences in the line profile shapes, we measure the relative velocities where the profiles of each of these lines reach a threshold amount of absorption. We first smooth the co-adds and calculate the velocity at which the absorption decreases to 80% and 60% of the continuum level. These velocities are marked in Figure 18, and are closer to the center of the line in the case of Fe II, confirming our qualitative statement that Mg II absorption extends to higher velocities. If we make the assumption that Fe and Mg have the same relative abundances and C_f at all gas velocities, this suggests that the density of the outflowing clouds decreases with increasing velocity, as the Fe II column decreases with density (see, e.g., Narayanan et al. 2008, for ionization modeling of Mg II absorbers).

8. DISCUSSION

8.1. Physical Characteristics of Outflows

8.1.1. Mg II

Similarly to W09, we use the ratio of the EWs on the blue sides of the Mg II lines to estimate a lower limit on the column density (N(Mg II)) in the outflowing gas. The oscillator strengths of the lines in the Mg II doublet have a ratio 2:1, and in the optically thin case the ratio of the EWs of the lines will also be 2:1. As the optical depth at line center (τ_0) increases and the lines become saturated, the EW ratio approaches 1:1; therefore the EW ratio can be used to constrain τ_0. Once τ_0 is known, N(Mg II) can be calculated using the equation from Spitzer (1968):

$$\log N = \log \frac{\mathrm{EW}}{\lambda} - \log \frac{2F(\tau_0)}{\pi^{1/2}\tau_0} - \log \lambda f - \log C_f + 20.053, \quad (8)$$

adjusted to include the effect of the covering fraction, C_f, where λ and EW are in Å, and N is in atoms cm^{-2}. $F(\tau_0)$ is given by

$$F(\tau_0) = \int_0^{+\infty} (1 - e^{-\tau_0 \exp(-x^2)})\, dx. \quad (9)$$

The EW ratio in the Mg II doublet is almost exactly equivalent to the "doublet ratio," $F(2\tau_0)/F(\tau_0)$. After this doublet ratio is calculated by taking the ratio of the EWs, one may numerically solve for τ_0. This method is strictly appropriate only when one absorbing cloud is considered. However, it has been found to yield good results even when the absorption is caused by a number of clouds if the optical depth in the weaker line is $\tau_0 < 5$ (Jenkins 1986).

We measure the EWs for the co-adds in the interval -384 km s^{-1} $< v < -200$ km s^{-1} for each line in the doublet; these measurements are listed in Table 2. We choose this interval to avoid measuring absorption at the systemic velocity, which is uncertain to within 200 km s^{-1} (see Section 2.3), and to avoid including absorption from the red side of the 2796 Å line in our 2803 Å line measurement. For the co-add of the entire sample, the EW ratio is 1.09 ± 0.16. This yields $\tau_{0,2803} \sim 3 - \infty$, where the lower limit corresponds to the 1σ upper limit on the EW ratio. In the case of the high-M_* co-add, the doublet ratio is 1.28 ± 0.16, which results in $\tau_{0,2803} \sim 1.4$–10. Using the equation for $\log N$ above, and assuming $C_f = 1$, we find $\log N(\mathrm{Mg\ II}) > 13.7$ for both the full sample and the high-M_* subsample. Assuming $C_f = 0.5$ increases $\log N$ by 0.3 dex.

To estimate a lower limit to N(H) in the outflow, we assume a more conservative value of $C_f = 1$, and we assume $N(\mathrm{Mg}) = N(\mathrm{Mg\ II})$; i.e., we do not apply an ionization correction. We assume the solar value for the abundance of Mg, $\log \mathrm{Mg/H} = -4.42$, and a factor of -1.3 dex Mg depletion onto dust (from Jenkins 2009, assuming $n(\mathrm{H}) \sim 1\,\mathrm{cm}^{-3}$). This yields a column density $\log N(\mathrm{H}) \gtrsim 19.4$. We emphasize that this is a very conservative lower limit on the column of outflowing gas because of our assumption about C_f, our neglect of ionization corrections, and because our method underestimates N for highly saturated Mg II-absorbing velocity components. In addition, emission from the Mg II 2796 transition may reduce the EW measured blueward of the Mg II 2803 transition, further reducing the calculated $\log N$(H). These results are nearly an order of magnitude smaller than the outflow column obtained in W09 ($\log N(\mathrm{H}) = 20.1$); however, this latter measurement was calculated using the EW ratio in the outflow line profile rather than in the observed profile, and used a wider range of velocities (-768 km s^{-1} $< v < 0$ km s^{-1}). This yielded higher EWs in each line and generally higher optical depths than our 1σ lower limits on τ.

We estimate the mass outflow rate by assuming a specific geometry for the outflowing gas. For a thin shell, the mass outflow rate is given by

$$\dot{M} \approx 22\ M_\odot\ \mathrm{yr}^{-1} C_f \frac{N(\mathrm{H})}{10^{20}\ \mathrm{cm}^{-2}} \frac{R}{5\ \mathrm{kpc}} \frac{v}{300\ \mathrm{km\ s}^{-1}} \quad (10)$$

from W09. The assumption for C_f is unimportant here, so long as it matches what was assumed for the calculation of N(H) (i.e., the factor of C_f cancels out). We have no constraint on the radial extent of the wind from our data (R), except that it is likely comparable to the size of the galaxies because C_f is high. For these purposes, we assume a minimum radius for the shell equal to the median half-light radius for the galaxy sample, 4.1 kpc. We use the velocity at 80% of the continuum in the co-add of all galaxies calculated as described in Section 7.2, -334 km s^{-1}. Note that this is *not* the same velocity measurement used in W09, who measured the velocity at 50% opacity in the outflow component after decomposing the line profile. The resulting mass outflow rate is $\dot{M} \gtrsim 5\ M_\odot$ yr^{-1}. As in previous work (e.g., Martin 1999; Rupke et al. 2005b; Martin 2005), we find that $\dot{M}$ is on the same order as the SFR of the sample ($\sim$1–30 $M_\odot$ yr^{-1}). We note that $\dot{M}$ in this sample is lower than in the W09 sample at $z \sim 1.4$, and that this is due to the smaller limit on the outflow N(H) derived from the TKRS co-adds. It may be that

the galaxies at lower z are less effective in driving outflows than at $z \sim 1.4$; however, we reiterate that the outflow N(H) in both this work and in W09 may be substantially underestimated.

8.1.2. Fe II

Because the profiles of the two Fe II lines do not have an asymmetric blue wing, we hypothesize that either these lines are too weak to trace outflows at velocities $\gtrsim$300 km s^{-1}, or alternatively that Fe II simply is not present in outflowing gas at these velocities. However, assuming the absorption on the blue sides of these lines at *lower* relative velocities is due to outflowing gas, we again use an EW ratio, this time in the velocity range -300 km s^{-1} $< v < -200$ km s^{-1}, to calculate a lower limit on the outflow column traced by Fe II. The EWs of the two lines in this velocity range for the co-add we use to analyze Fe II are both EW $= 0.14 \pm 0.06$, yielding an observed EW ratio of 1.0 ± 0.7. The two Fe II lines have oscillator strengths in the ratio 3.475:1. We numerically solve the equation $F(3.475\tau_0)/F(\tau_0) = 1.0 \pm 0.7$ for $\tau_{0,2586}$ and obtain the limit $\tau_{0,2586} \gtrsim 1.5$. Using $\log \lambda_{2586} f = 2.252$ (Morton 2003) and EW$_{\rm blue}$(2586) = 0.08–0.2 Å, we find $\log N$(Fe II) $\gtrsim$ 13.5–13.9. Assuming solar abundance, no ionization correction and a factor of -2.3 dex depletion onto dust (Jenkins 2009), we obtain $\log N$(H) $\sim$ 20.3–20.7, which is nearly a factor of 10 higher than our constraint on the column from analysis of Mg II. As in Martin & Bouché (2009), analysis of the Fe II profiles yields a more stringent constraint on the outflow column than analysis of Mg II.

We may compare column densities measured in different relative velocity ranges for these lines if we assume that the distribution of N in individual clouds changes smoothly with changing velocity *and* if we assume that the C_f of the outflow is constant at all velocities. We calculate a 3σ upper limit of $\sim$0.3 Å on the EW of absorption at velocities -500 km s^{-1} $< v < -300$ km s^{-1} with respect to both Fe II absorption lines. We use this measurement to set an upper limit on the outflow column at these velocities by assuming that this gas must have an optical depth lower than the limit determined above for the range -300 km s^{-1} $< v < -200$ km s^{-1}. We again use the equation for $\log N$ given in the previous section, with $\tau_{0,2600} = 3.475\tau_{0,2586} = 5.2$ and $\log \lambda_{2600} f = 2.793$ (Morton 2003). We find $\log N$(FeII) < 13.8 and $\log N$(H) < 20.6, using the same assumptions for abundance, ionization correction, and dust depletion as above. Note that this result requires that $C_f = 1$ at all velocities; this assumption does not hold for the ULIRG outflows discussed in Martin & Bouché (2009).

8.2. Outflow Absorption Dependence on SFR and M_*

We have shown that outflow absorption strength increases with SFR$_{\rm UV}$ and M_* in the TKRS sample. This statement addresses the behavior of outflow absorption in the middle- and high-SFR$_{\rm UV}$ and M_* subsamples only (with S/N $>$ 6 pixel^{-1}); in the subsamples with the lowest values of these parameters, the co-adds have S/N $\sim$ 3 pixel^{-1} and only poorly constrain outflow properties. While the lowest-M_* subsample technically has an outflow EW large enough to be significant ($>$1.8 Å; see discussion in Section 4.3), the low measurement of $W_{\rm diff}$ is consistent with no outflow.

Interestingly, both the middle-SFR$_{\rm UV}$ and M_* subsamples have $W_{\rm diff}$ ($\sim$0.2–0.3 Å) and outflow EW ($\sim$0.8–1.0 Å) measurements consistent with no outflow. These co-adds have S/N $\sim$ 6 pixel^{-1}; in the simulated spectra discussed in Section 4.3, saturated ("strong") outflows with $v \gtrsim 200$ km s^{-1} and $b_D \gtrsim 150$ km s^{-1} yield values of outflow EW greater than 1.4 Å with 95% confidence. Certainly weaker outflows with smaller b_D, velocities $<$100 km s^{-1}, and with column densities such that the total EW(Mg II 2796) $\lesssim$ 3.5 Å, would not be detected in these co-adds, and such outflows could exist in these galaxies. However, we find that the middle subsamples of galaxies with $0.555 < \log {\rm SFR_{UV}} < 0.942$ and $9.86 < \log M_* < 10.49$ are not driving strong outflows at $z \sim 1$.

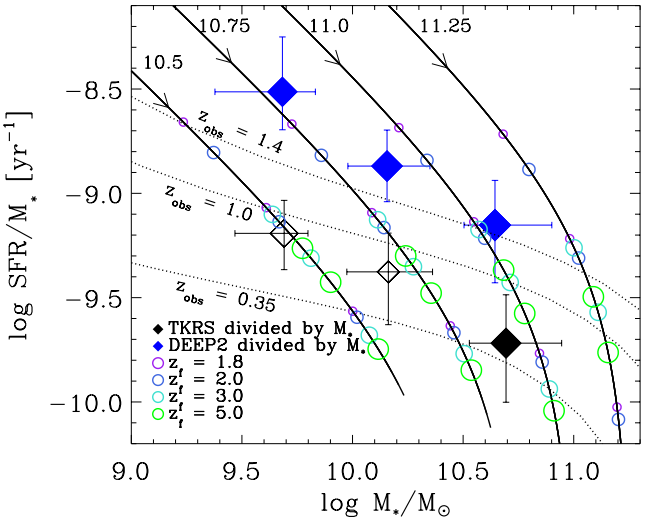

Figure 19. Diamonds show SSFR vs. M_* for the W09 and TKRS subsamples divided by M_* (blue and black, respectively). The point size is scaled to the square root of the outflow EW for each subsample. Errorbars show the $\pm$34th percentile values of SSFR and M_* for each subsample. The open diamonds indicate subsamples for which analysis of the low-S/N co-adds provides only a tentative detection or an upper limit on the outflow EW. Dotted lines show fits to the SSFR–M_* main sequence derived in Noeske et al. (2007b) at $z_{\rm obs} = 0.35$, 1, and 1.4 (bottom to top). Solid lines show the paths of τ model galaxies through the diagram with time for $\log M_b = 10.5$, 10.75, 11.0, and 11.25 (left to right). The open circles along these lines indicate the location of individual models with different formation redshifts (z_f) at $z_{\rm obs} = 0.35$, 1.0, and 1.4. Each color corresponds to a model with a different formation redshift, and thus generally appears three times along each solid line (i.e., there is one circle of each color for each observed redshift). See the text for more details.

(A color version of this figure is available in the online journal.)

Spectra of galaxies with M_* and SFR$_{\rm UV}$ above these ranges show clear evidence for outflow. This includes galaxies in our subsample specifically selected to have similar SFR$_{\rm UV}$ and M_* to the W09 sample at $z \sim 1.4$ (the "DEEP2-like" subsample). It also includes the galaxies in the W09 sample, which all have $\log {\rm SFR_{UV}} \gtrsim 1$. Our middle-$M_*$ subsample overlaps with the W09 sample in M_* but falls below it in SFR$_{\rm UV}$, *suggesting that outflow absorption strength is more strongly correlated with SFR than with M_* at z = 1–1.4*. We also note that outflow absorption strength in general does not increase with increasing SSFR. Figure 19 shows the SSFR–M_* distribution of the TKRS and W09 M_*-divided samples with black and blue diamonds, respectively. Although the middle-M_* TKRS subsample has higher SSFR than the high-M_* TKRS subsample, it exhibits no outflow signature (see Figures 10 and 11).

It is interesting to consider whether outflowing gas will escape from these high-M_* and high-SFR$_{\rm UV}$ galaxies. The escape velocity of galaxies can be estimated from the width of the [O II] emission line as in W09. The [O II] linewidths (σ) of TKRS galaxies were measured in Weiner et al. (2006). We find that the median σ for both our high-M_* and high-SFR$_{\rm UV}$ subsamples is

$\sigma([\mathrm{O\,II}]) = 80$ km s^{-1}, and use the relation from W09:

$$V_{\mathrm{escape}} \approx 5 - 6\sigma([\mathrm{O\,II}]). \quad (11)$$

This yields an escape velocity ∼480 km s^{-1}. From the outflow profiles plotted in green in the bottom panels of Figure 10, we see that in the high-SFR$_{\mathrm{UV}}$ subsample, which is most similar to the W09 sample in terms of SFR, a tail of Mg II absorption extends beyond the escape velocity. In the other subsamples, there is no compelling evidence for gas beyond the escape velocity. We conclude that is it unlikely that the gas detected in absorption is able to escape from most of the galaxies in our sample. This differs from the results of W09, who find that the absorption line profile extends well beyond the median escape velocity for each of their M_*-divided subsamples. The profile extends to particularly high velocities in the highest-M_* galaxies; the velocity where the profile is at 90% of the continuum level exceeds the escape velocities for >84% of the subsample with $\log M_* > 10.45$. We cannot conclude from this analysis, however, that cool Mg II- absorbing gas does not escape from the bulk of the TKRS sample at $z \sim 1$. Martin & Bouché (2009) found that in low-ionization ULIRG outflows, the absorption is saturated at all velocities, while the C_f of the gas decreases with increasing outflow velocity. This implies that the velocity extent of the detected absorption profile is controlled by the decreasing gas C_f and the S/N of the data, rather than decreasing N at high velocities, and that there may be dense clouds with low C_f moving at well above the escape velocity. Higher S/N co-adds are needed to constrain the absorption depth at the escape velocity more precisely. Hotter, and likely more diffuse, gas kinematics are not constrained by our observations or those of W09.

8.3. Trends in Outflow Absorption with Σ_{SFR}

As discussed in Section 1, Heckman (2002) noted that local galaxies which drive winds strong enough to be detectable in absorption universally satisfy the criterion $\Sigma_{\mathrm{SFR}} > 0.1\,M_\odot$ yr^{-1} kpc^{-2}. The galaxies in the W09 sample and LBGs at $z \sim 2$–3 (Shapley et al. 2003; Pettini et al. 2002) also meet this criterion. Further evidence for a threshold Σ_{SFR} is provided by studies of outflow remnants in emission. For instance, in a study of the relationship between the sizes of radio halos created by energy input from star formation and the sizes of star-forming regions in local spiral galaxies, Dahlem et al. (2006) found that radio halo size is linearly correlated with the size of star-forming regions. They additionally found that there is a threshold energy input rate per unit surface area above which radio halos may form, and that this threshold depends on the mass surface density of the galaxy.

There are two different physical mechanisms that may be responsible for driving these winds, which result in different dependences of outflow properties on Σ_{SFR}. One mechanism is the thermalization of energy from supernova ejecta, which generates a hot wind that entrains cold clouds in an outflow via ram pressure (e.g., Chevalier & Clegg 1985; Heckman et al. 1990). McKee & Ostriker (1977) suggested that a threshold spatial density of supernovae must be achieved in order for this mechanism to operate. Regions with supernovae densities above such a threshold create and maintain a superbubble filled with hot gas with a cooling timescale much longer than the bubble expansion time (Heckman et al. 1990). Further, at higher supernova rate per unit volume (or at lower ambient gas density), radiative losses in the bubble are reduced, and the efficiency of thermalization of the ejecta is enhanced (Heckman et al. 1990; Strickland & Heckman 2009). This spatial supernova rate density is closely tied to the observable quantity, Σ_{SFR}. Additionally, as described by Martin (2005) and Murray et al. (2005), in this energy-driven paradigm, the terminal velocity of cold clouds in the outflow is proportional to $R_0^{-0.5}$, where R_0 is the size of the starburst.

The other mechanism that may be important in driving winds is momentum from radiation pressure or cosmic ray pressure generated by a starburst or AGN (Murray et al. 2005; Socrates et al. 2008). In the case of radiation-driven outflow, the dependence of outflow velocity on starburst radius for an optically thick wind is slightly weaker, $(\ln 1/R_0)^{0.5}$, while the criterion that must be met to drive a wind depends on the masses of the luminous star clusters driving the outflow. The star cluster mass, like spatial supernova density, is closely related to Σ_{SFR} (see Murray et al. 2010 for further discussion). Thus, while both proposed mechanisms require that a threshold Σ_{SFR} be satisfied to take effect, the empirical relationship between outflow velocity and starburst radius may eventually help constrain the relative contributions of these two mechanisms for driving outflows, although these relationships are complicated by additional factors (e.g., viewing angle, outflow morphology and C_f, detection technique and sensitivity).

Our sample weakly suggests that outflow absorption strength increases with Σ_{SFR}. As in Section 8.2, although we measure relatively high values of outflow EW for our lowest-Σ_{SFR} co-add (with $\log \Sigma_{\mathrm{SFR}} < -1.36$), because this spectrum has low S/N, we consider the detection of outflow tentative, and it must be confirmed in future analyses. In the middle and high-Σ_{SFR} subsamples, the difference between outflow absorption measurements is significant only when comparing the values of W_{diff}; the outflow EW values/limits are consistent within the errors. It is interesting, though at the limit of our data, to test whether the local "threshold" on Σ_{SFR} for the driving of outflows is also physically relevant at $z \sim 1$. By accounting for a possible systematic underestimate of SFR by 0.21 dex (see Section 5.4), we have constructed a subsample with a Σ_{SFR} that is likely to be under the local threshold in the mean. This co-add has S/N ∼ 4.7 pixel^{-1} and yields an outflow EW ∼1.6 Å. This value is suggestive of outflow, given the results of our analysis in Section 4.3, although the outflow absorption strength is not as large as in the high-M_* and high-SFR$_{\mathrm{UV}}$ subsamples. However, given the *minimum* estimated dispersion in our SFRs of 0.43 dex, this subsample may include some galaxies with $\Sigma_{\mathrm{SFR}} \gtrsim 0.1\,M_\odot$ yr^{-1} kpc^{-2}.

Additionally, we have measured only a flux-averaged Σ_{SFR}, with galaxy sizes parameterized by the half-light radius in the UV. Starburst radii in the local universe are often constrained using half-light radii measured from UV or Hα imaging; however, local and distant starbursts have distinct morphologies which may make measurements of half-light radii less appropriate for our purposes at $z \sim 1$. For instance, local LIRGs commonly have centrally concentrated star formation (Sanders & Mirabel 1996), while LIRGs at $z \sim 1$ have more widely distributed star-forming knots (Melbourne et al. 2008). The half-light radius, therefore, may not accurately characterize the starburst radius in distant galaxies, where it reflects the sizes of the distributions of star-forming knots in the objects, rather than the total surface area of the knots themselves. Although we have not detected a strong dependence of outflow absorption strength on Σ_{SFR}, we have by no means ruled it out, and future studies with higher

S/N spectra should include more detailed analyses of $\Sigma_{\rm SFR}$ in distant galaxies.

8.4. Temporal Evolution of Outflows

8.4.1. Following the Sample Evolution

We have identified evolutionary trends in outflow absorption strength which are dependent on galaxy M_*. Specifically, we have found that at $\log M_* \gtrsim 10.49$, outflows are of comparable strength at $z \sim 1$ and 1.4. At lower M_*, however, there is a significant decrease in outflow absorption strength with decreasing redshift as well as a decrease in the SFR in the same galaxies. Stated in another way, galaxies with similar SFRs at $z \sim 1$ and 1.4 have similarly large outflow absorption strengths, while galaxies with $\log {\rm SFR_{UV}} < 0.942$ ($<8.7\,M_\odot$ yr^{-1}) do not appear to drive strong outflows. While these conclusions apply to galaxies in specific M_* and $\rm SFR_{UV}$ ranges at different redshifts, they do not address the evolution of the outflow properties in a given galaxy through time. We now attempt to associate the TKRS galaxies with their progenitors in the W09 sample at $z \sim 1.4$ by invoking so-called τ models to parameterize the evolution of SFR and M_* in a given galaxy. We are largely motivated by the success of τ models in reproducing the distribution of galaxies in SSFR–M_* space out to $z \sim 1$ (Noeske et al. 2007b). These models are too simplistic to fully describe the evolution of an individual galaxy, which may experience starbursts, mergers, and other disturbances that define its star formation history. However, τ models were intended to describe the broad evolution of populations of galaxies, and are appropriate here, as we are interested in the evolution of large galaxy subsamples.

In the context of this model, the SFR of a galaxy of total baryonic mass M_b at redshift z is given by

$$\mathrm{SFR}(M_b, z) = \mathrm{SFR}(z_f) \exp\left[-\frac{T}{\tau}\right], \quad (12)$$

where z_f is the formation redshift of the galaxy, $T = t(z) - t(z_f)$ is the galaxy age, and τ is the e-folding time. Noeske et al. (2007b) found that models with

$$\tau(M_b) = c_\alpha M_b^\alpha \quad (13)$$

and

$$1 + z_f(M_b) = c_\beta M_b^\beta \quad (14)$$

with the constants $10^{20.4} \leqslant c_\alpha \leqslant 10^{20.7}$, $10^{-2.5} \leqslant c_\beta \leqslant 10^{-1.7}$, $\alpha = -1$, and $\beta = 0.3$ successfully reproduce the SSFR–M_* "main sequence" as well as the spread around this sequence for galaxies drawn from the AEGIS survey at $0.2 < z < 1.1$. The changing dependence of z_f on M_b is necessary to account for the high SSFRs of galaxies at low M_*. Although these models have not been tested out to $z \sim 1.4$, where the AEGIS sample is incomplete even at the highest M_*, we assume that they fully describe the locus of star-forming galaxies at this redshift.

Figure 19 shows the location in SSFR–M_* space of the W09 M_*-divided subsamples (blue diamonds) and the TKRS M_*-divided subsamples (black diamonds). The point size increases with the square root of the outflow EW for each subsample. The open diamonds indicate the location of the TKRS subsamples which do not yield an outflow detection with high confidence. The errorbars indicate the spread in galaxy properties in each subsample at the ±34th percentiles. The loci of the SSFR–M_* "main sequence" at observed redshifts $z_{\rm obs} = 0.35$, 1.0, and 1.4 are shown with nearly horizontal dotted lines from bottom to top. These loci describe the locations of galaxies in the AEGIS sample of Noeske et al. (2007b) at $z < 1.1$. The four solid lines show the paths of τ model galaxies of various M_b (with models for $\log M_b = 10.5$, 10.75, 11.0, and 11.25 plotted from left to right). The circles along the single τ model paths mark the locations of model galaxies with different formation redshifts (z_f) at observed redshifts $z_{\rm obs} = 0.35$, 1.0, and 1.4. The figure legend gives the appropriate z_f for each color; for instance, purple circles are for the latest $z_f = 1.8$ models, and green circles are for the earliest $z_f = 5.0$ models.

The W09/DEEP2 galaxies lie slightly above the SSFR–M_* main sequence at $z \sim 1.4$. This is because the DEEP2 R-band selection limits the sample to the highest-SFR galaxies at a given M_*; the effect is most severe at $z = 1.4$, the redshift limit of the survey. (As noted previously, the model for the main sequence at $z \sim 1.4$ has not been observationally tested and is an extrapolation from lower redshift models.) The TKRS galaxies, on the other hand, lie below the main sequence at $z \sim 1$. This discrepancy may be due to a number of factors. Noeske et al. (2007a) used a combination of $L_{\rm IR}$ and emission line luminosities to constrain the total extinction-corrected SFRs in their sample. We have shown that our UV-based SFRs are systematically lower (by 0.21 dex) than IR-based SFRs for galaxies with IR detections; thus, there may be a systematic offset between the SFRs in this work and in Noeske et al. (2007a). In addition, we may have failed to remove some red, non-star-forming galaxies from the highest-M_* subsample, which would reduce the median SFR in this bin. While the offset between the main sequence and our sample is as large as ∼0.25 dex in SSFR for the highest-M_* subsample, this discrepancy does not significantly affect our conclusions, discussed below.

8.4.2. Outflows in the Sample Progenitors

We first consider the highest-M_* TKRS subsample. The median galaxy in this sample has $z_f \sim 5$; i.e., it lies near the green model along the $\log M_b = 11.0$ evolutionary track at $z_{\rm obs} = 1$. In the case that we are underestimating the sample SFR by ∼0.2 dex, the median galaxy would lie near the cyan model with $z_f \sim 3$. The highest-M_* W09 subsample appears to include the progenitor of this median galaxy (the green or cyan models at $z_{\rm obs} = 1.4$), as well as the highest SSFR galaxies in the subsample (with later z_f). It appears that outflows persist at similar strengths in high M_* galaxies between $z = 1.4$ and $z \sim 1$. Even massive galaxies with early $z_f \gtrsim 5$ and very low SSFRs are apparently still driving outflows at $z \sim 1$. It is interesting to consider that detection of the presence of outflows depends not only on the kinematic properties of the ongoing flow, but also on the amount of gas that remains available in the ISM for acceleration. This depends, in principle, on the star formation history of the galaxy and the amount of gas mass which has been converted into stars, the strength of past outflows, and whether or not these outflows exceed the galaxy escape velocity. Although the high-M_* galaxies in our sample are driving strong outflows and apparently losing some of this gas at $z \sim 1.4$ (W09), they retain enough cool gas until $z \sim 1$ to continue driving outflows at these later epochs.

We next turn to the lower-M_* subsamples. The high-SSFR galaxies in the middle-M_* TKRS subsample lie close to the $\log M_b = 10.75$ evolutionary track. There are W09 galaxies that lie along this track (in the lowest- or middle-M_* W09

subsample) which have SSFRs that are likely consistent with progenitors of these high-SSFR TKRS galaxies, particularly if we consider that our SSFR values may be systematically low. That is, a τ model galaxy with $\log M_b = 10.75$ and $z_f = 2$ (shown with blue circles) may be included in the middle-M_* W09 subsample when it is observed at $z_{\rm obs} = 1.4$ and passes through the location of the middle-M_* TKRS subsample at $z_{\rm obs} = 1$. In the case that we are underestimating the SSFR of this subsample, the middle-M_* galaxies at $z \sim 1$ will lie close to the purple model with $z_f = 1.8$; the progenitors of this model pass through the lowest-M_* W09 subsample at $z_{\rm obs} = 1.4$. The galaxies with the *lower* SSFR values in this middle-M_* TKRS subsample, however, have no counterpart in W09. We cannot constrain with this analysis what fraction of the galaxies in this subsample have progenitors in the W09 sample. However, the W09 galaxies were found to ubiquitously host outflows, while the middle-M_* TKRS subsample does not host strong outflows. It is unclear whether the outflows at $z \sim 1.4$ have been shut off by $z \sim 1$, or if the lack of outflows in lower-SSFR galaxies is diluting the outflow signature.

The galaxies in the lowest-M_* TKRS subsample may have a few progenitors in the low-M_* end of the lowest-M_* W09 subsample; i.e., there are a few W09 galaxies that lie between the $\log M_b = 10.5$ and 10.75 evolutionary tracks. However, we do not comment on the presence or the absence of outflows in these galaxies at $z \sim 1$, as we lack robust outflow measurements for this subsample due to the low S/N ~ 2.3 pixel^{-1} of the co-add.

In summary, we find that outflows persist in galaxies with $\log M_* \gtrsim 10.5$ between $z \sim 1.4$ and 1, likely due to their consistently high absolute SFRs, while in our middle-M_* subsample, outflows may have shut down during this time. We lack the S/N to comment on the evolution of outflows in the lowest-M_* TKRS galaxies.

8.4.3. The Sample Descendants

Sato et al. (2009) investigated outflows traced by Na I absorption in AEGIS galaxies at $0.11 < z < 0.54$. Keeping in mind the caveat that Na I likely traces cooler, higher density gas than Mg II, we may search for the descendants of TKRS galaxies in the Sato et al. (2009) sample and compare outflow properties. Sato et al. (2009) are able to measure outflow properties only in galaxy spectra with the highest S/N near the Na I doublet; these are the highest-S/N spectra in the sample of Noeske et al. (2007a, 2007b). As a result, the Sato et al. (2009) study is complete only down to $\log M_* \gtrsim 10.75$ and only at the lowest redshifts ($z \lesssim 0.3$). Among these galaxies, the vast majority have Na I absorption at the galaxy systemic velocity, or redshifted with respect to systemic velocity. At $z > 0.3$, the galaxy spectra with sufficient S/N to measure Na I kinematics exhibit a mix of outflows, inflows, and absorption at systemic velocity. These galaxies are massive enough to be descendants of the galaxies in the high-M_* W09 and TKRS subsamples, and yet do not appear to be driving Na I outflows ubiquitously, particularly at the lowest redshifts. It may be that either these galaxies are driving outflows of slightly warmer gas with lower density than can be probed by Na I, or that their outflows have been halted, possibly because the ISM has been removed. These galaxies have lower SFRs than massive galaxies at $z \sim 1$, consistent with the idea that their cool gas supply has been reduced or exhausted.

In galaxies with $\log M_* < 10.75$, many of which may be descendants of the lower-M_* TKRS subsamples, there is again a range in Na I kinematics. Most of the galaxies with kinematic information available are not driving outflows; however, many more have gas kinematics which have not been measured. Thus, the outflow properties of the descendants of the lower-M_* TKRS galaxies remain unconstrained.

Many of the galaxies in the TKRS sample, like those in the W09 sample, have $\log M_* < 10.7$; i.e., they are below the "quenching mass" derived by Bundy et al. (2006) for $0.4 < z < 0.7$. This quenching mass describes the mass at which star formation is suppressed and decreases from $z = 1.4$ to 0.4. These lower-M_* galaxies are not driving strong winds for the most part, and because they are well below the quenching limit, are likely to remain blue, star-forming galaxies today. The TKRS galaxies with M_* above this limit will likely evolve to the red sequence by $z = 0$.

9. CONCLUSIONS

We have analyzed the spectra of 468 galaxies in the TKRS survey (Wirth et al. 2004) of the GOODS-N field at $0.7 < z < 1.5$ and identified cool outflowing gas traced by Mg II absorption in both individual galaxy spectra and in co-added spectra. This is the first report of cool outflows in this redshift range. We find that the most massive, highest-SFR galaxies in the sample exhibit a strong outflow absorption signature, while less massive ($\log M_* \lesssim 10.5$, $\log {\rm SFR_{UV}} < 0.94$) star-forming galaxies have no outflows or outflows with $v \lesssim 100$ km s^{-1} and with $b_D \lesssim 150$ km s^{-1}. These same low-M_* galaxies have higher specific SFRs (SSFRs) than the high-M_* subsample, but lower absolute SFRs, suggesting that outflow absorption strength is more closely correlated with the absolute SFR than either M_* or SSFR.

We find that the outflowing gas has a column density $\log N({\rm H}) > 19.4$, which yields a mass outflow rate of order the SFR of our sample. This column is slightly smaller than the outflow column densities observed at $z \sim 1.4$ in the DEEP2 survey (W09) and in local IR luminous galaxies (e.g., Rupke et al. 2005a). Our comparison of the Fe II and Mg II line profiles in co-added spectra of high-SFR galaxies suggests that Mg II emission is a common feature of galaxies in this sample. Although it remains unclear whether the observed Fe II absorption traces outflowing gas, by making the assumption that Fe II is indeed present in the same outflowing clouds that are traced by Mg II and that the C_f is independent of outflow velocity, we use the lack of Fe II absorption blueward of -300 km s^{-1} to place an upper limit on the outflow column density at these velocities of $\log N({\rm H}) \sim 20.6$.

We also investigate, for the first time, trends in outflow absorption strength with SFR surface density ($\Sigma_{\rm SFR}$) at $z \sim 1$. We find weak evidence for a slight increase in outflow absorption with increasing $\Sigma_{\rm SFR}$ at $\log \Sigma_{\rm SFR} > -1.36$. We cannot rule out outflows in galaxies with $\Sigma_{\rm SFR}$ below the local threshold for driving winds, $\Sigma_{\rm SFR} = 0.1\ M_\odot$ yr^{-1} kpc^{-2}, and in fact see some evidence for outflows in these objects. Future work in this area should focus on developing a set of measurements of the surface area over which star formation occurs, carefully calibrated total SFRs, and outflow velocities in individual galaxies.

Finally, we examine the temporal evolution of outflows. We find that galaxies with similar SFRs at $z \sim 1.4$ and $z \sim 1$ have similarly strong outflow absorption. To examine the evolution of outflows in specific galaxies through time, we invoke the τ model star formation histories of Noeske et al. (2007b), who note that the decline in SFR at a given M_* with time is consistent with being driven by gas exhaustion. We find that outflows persist in

massive ($\log M_*/M_\odot \gtrsim 10.5$) galaxies between $z \sim 1.4$ and $z \sim 1$, in spite of a decreasing SFR between these two epochs. Measurements of Na I kinematics at $z \sim 0.2$ (Sato et al. 2009) suggest that these massive galaxies, whose SFRs will continue to decline over time, will stop driving winds at low redshift. We speculate that this is because the cool gas supply in the ISM will be exhausted by $z \sim 0.2$. Many (but not all) of these galaxies will become red and dead ellipticals by this time. We measure weak or no outflows (with outflow $v \lesssim 100$ km s^{-1}) in galaxies with lower masses at $z \sim 1$. Based on our comparison of the SSFR and M_* of our sample to those of τ model galaxies with exponentially declining star formation histories, we find that the progenitors of some of these lower-M_* galaxies are likely contained in the DEEP2 $z \sim 1.4$ comparison sample and are driving strong outflows at $z \sim 1.4$. These objects are likely to remain blue cloud galaxies until $z \sim 0$. It appears that the outflow strength or the frequency of outflows in this population has declined from $z \sim 1.4$ to $z \sim 1$, as has the SFR. It is undetermined whether they will ever drive strong outflows as they evolve from $z \sim 1$ to today.

K.H.R.R. and D.C.K. acknowledge support for this project from NSF grants AST 08-08133 and AST 05-07483. B.J.W. has been supported by NASA/Spitzer contract 1255094. J.X.P. acknowledges funding though an NSF CAREER grant (AST 05-48180).

The authors thank J. Melbourne for providing measurements of galaxy radii and IR luminosities, K. Bundy for providing measurements of M_*, and J. Lotz for providing morphological measurements. We thank the TKRS team for making their catalogs and spectra publicly available. We acknowledge the anonymous referee, whose suggestions helped to improved this paper. Finally, we thank Jennifer Lotz, Brice Ménard, Kai Noeske, and David Rupke for interesting and helpful discussions during the analysis of these results.

The authors recognize and acknowledge the very significant cultural role and reverence that the summit of Mauna Kea has always had within the indigenous Hawaiian community. We are most fortunate to have the opportunity to conduct observations from this mountain.

Facilities: Keck:II (DEIMOS), *HST* (ACS)

REFERENCES

Ajiki, M., et al. 2002, ApJ, 576, L25
Bell, E. F., McIntosh, D. H., Katz, N., & Weinberg, M. D. 2003, ApJS, 149, 289
Bell, E. F., et al. 2005, ApJ, 625, 23
Blanton, M. R. 2006, ApJ, 648, 268
Bond, N. A., Churchill, C. W., Charlton, J. C., & Vogt, S. S. 2001, ApJ, 562, 641
Bouché, N., Murphy, M. T., Péroux, C., Csabai, I., & Wild, V. 2006, MNRAS, 371, 495
Bouché, N., Murphy, M. T., Péroux, C., Davies, R., Eisenhauer, F., Förster Schreiber, N. M., & Tacconi, L. 2007, ApJ, 669, L5
Bundy, K., Ellis, R. S., & Conselice, C. J. 2005, ApJ, 625, 621
Bundy, K., et al. 2006, ApJ, 651, 120
Capak, P., et al. 2004, AJ, 127, 180
Chevalier, R. A., & Clegg, A. W. 1985, Nature, 317, 44
Churchill, C. W., Mellon, R. R., Charlton, J. C., Jannuzi, B. T., Kirhakos, S., Steidel, C. C., & Schneider, D. P. 2000, ApJS, 130, 91
Coil, A. L., et al. 2004, ApJ, 609, 525
Cooksey, K. L., Prochaska, J. X., Chen, H.-W., Mulchaey, J. S., & Weiner, B. J. 2008, ApJ, 676, 262
Cowie, L. L., & Barger, A. J. 2008, ApJ, 686, 72
Dahlem, M., Lisenfeld, U., & Rossa, J. 2006, A&A, 457, 121
Davis, M., et al. 2003, in Proc. SPIE, 4834, 161
Dekel, A., & Silk, J. 1986, ApJ, 303, 39
Dutton, A. A., & van den Bosch, F. C. 2009, MNRAS, 396, 141
Faber, S. M., et al. 2003, Proc. SPIE, 4841, 1657
Faber, S. M., et al. 2007, ApJ, 665, 265
Frye, B., Broadhurst, T., & Benítez, N. 2002, ApJ, 568, 558
Giavalisco, M., et al. 2004, ApJ, 600, L93
Glazebrook, K., Offer, A. R., & Deeley, K. 1998, ApJ, 492, 98
Heckman, T. M. 2002, in ASP Conf. Ser. 254, Extragalactic Gas at Low Redshift, ed. J. S. Mulchaey & J. T. Stocke (San Francisco, CA: ASP), 292
Heckman, T. M., Armus, L., & Miley, G. K. 1990, ApJS, 74, 833
Heckman, T. M., Lehnert, M. D., Strickland, D. K., & Armus, L. 2000, ApJS, 129, 493
Hopkins, A. M. 2004, ApJ, 615, 209
Hopkins, P. F., Hernquist, L., Cox, T. J., & Kereš, D. 2008, ApJS, 175, 356
Jenkins, E. B. 1986, ApJ, 304, 739
Jenkins, E. B. 2009, ApJ, 700, 1299
Kennicutt, R. C., Jr. 1998, ARA&A, 36, 189
Kinney, A. L., Bohlin, R. C., Calzetti, D., Panagia, N., & Wyse, R. F. G. 1993, ApJS, 86, 5
Lamers, H. J. G. L. M., & Cassinelli, J. P. 1999, Introduction to Stellar Winds (Cambridge: Cambridge Univ. Press)
Le Floc'h, E., et al. 2005, ApJ, 632, 169
Lehnert, M. D., & Heckman, T. M. 1995, ApJS, 97, 89
Lehnert, M. D., & Heckman, T. M. 1996, ApJ, 472, 546
Lotz, J. M., Jonsson, P., Cox, T. J., & Primack, J. R. 2008, MNRAS, 391, 1137
Lotz, J. M., Madau, P., Giavalisco, M., Primack, J., & Ferguson, H. C. 2006, ApJ, 636, 592
Lotz, J. M., Primack, J., & Madau, P. 2004, AJ, 128, 163
Maller, A. H., & Bullock, J. S. 2004, MNRAS, 355, 694
Martin, C. L. 1999, ApJ, 513, 156
Martin, C. L. 2005, ApJ, 621, 227
Martin, C. L. 2006, ApJ, 647, 222
Martin, C. L., & Bouché, N. 2009, ApJ, 703, 1394
McKee, C. F., & Ostriker, J. P. 1977, ApJ, 218, 148
Melbourne, J., Koo, D. C., & Le Floc'h, E. 2005, ApJ, 632, L65
Melbourne, J., Phillips, A. C., Harker, J., Novak, G., Koo, D. C., & Faber, S. M. 2007, ApJ, 660, 81
Melbourne, J., et al. 2008, AJ, 135, 1207
Ménard, B., & Chelouche, D. 2009, MNRAS, 393, 808
Meurer, G. R., Heckman, T. M., Lehnert, M. D., Leitherer, C., & Lowenthal, J. 1997, AJ, 114, 54
Morton, D. C. 2003, ApJS, 149, 205
Murray, N., Martin, C. L., Quataert, E., & Thompson, T. A. 2007, ApJ, 660, 211
Murray, N., Ménard, B., & Thompson, T. A. 2010, arXiv:1005.4419
Murray, N., Quataert, E., & Thompson, T. A. 2005, ApJ, 618, 569
Narayanan, A., Charlton, J. C., Misawa, T., Green, R. E., & Kim, T.-S. 2008, ApJ, 689, 782
Noeske, K. G., et al. 2007a, ApJ, 660, L47
Noeske, K. G., et al. 2007b, ApJ, 660, L43
Pettini, M., Rix, S. A., Steidel, C. C., Adelberger, K. L., Hunt, M. P., & Shapley, A. E. 2002, ApJ, 569, 742
Pettini, M., Shapley, A. E., Steidel, C. C., Cuby, J.-G., Dickinson, M., Moorwood, A. F. M., Adelberger, K. L., & Giavalisco, M. 2001, ApJ, 554, 981
Phillips, A. C. 1993, AJ, 105, 486
Rodríguez-Merino, L. H., Chavez, M., Bertone, E., & Buzzoni, A. 2005, ApJ, 626, 411
Rubin, K. H. R., Prochaska, J. X., Koo, D. C., Phillips, A. C., & Weiner, B. J. 2010, ApJ, 712, 574
Rupke, D. S., Veilleux, S., & Sanders, D. B. 2005a, ApJS, 160, 87
Rupke, D. S., Veilleux, S., & Sanders, D. B. 2005b, ApJS, 160, 115
Sanders, D. B., & Mirabel, I. F. 1996, ARA&A, 34, 749
Sato, T., Martin, C. L., Noeske, K. G., Koo, D. C., & Lotz, J. M. 2009, ApJ, 696, 214
Schwartz, C. M., & Martin, C. L. 2004, ApJ, 610, 201
Seibert, M., et al. 2005, ApJ, 619, L55
Shapley, A. E., Steidel, C. C., Pettini, M., & Adelberger, K. L. 2003, ApJ, 588, 65
Snow, T. P., Lamers, H. J. G. L. M., Lindholm, D. M., & Odell, A. P. 1994, ApJS, 95, 163
Socrates, A., Davis, S. W., & Ramirez-Ruiz, E. 2008, ApJ, 687, 202
Spitzer, L. 1968, Diffuse Matter in Space (New York: Interscience)

Steidel, C. C., Giavalisco, M., Dickinson, M., & Adelberger, K. L. 1996, AJ, 112, 352
Strauss, M. A., et al. 2002, AJ, 124, 1810
Strickland, D. K., & Heckman, T. M. 2009, ApJ, 697, 2030
Strickland, D. K., Heckman, T. M., Colbert, E. J. M., Hoopes, C. G., & Weaver, K. A. 2004, ApJ, 606, 829
Strickland, D. K., & Stevens, I. R. 2000, MNRAS, 314, 511
Tinker, J. L., & Chen, H.-W. 2008, ApJ, 679, 1218
Tremonti, C. A., Moustakas, J., & Diamond-Stanic, A. M. 2007, ApJ, 663, L77
Treyer, M., et al. 2007, ApJS, 173, 256
Veilleux, S., Cecil, G., & Bland-Hawthorn, J. 2005, ARA&A, 43, 769
Wang, B. 1993, ApJ, 415, 174
Weiner, B. J., et al. 2005, ApJ, 620, 595
Weiner, B. J., et al. 2006, ApJ, 653, 1027
Weiner, B. J., et al. 2009, ApJ, 692, 187
Willmer, C. N. A., et al. 2006, ApJ, 647, 853
Wirth, G. D., et al. 2004, AJ, 127, 3121